

# Sub-stellar fragmentation in self-gravitating fluids with a major phase transition

A. Füglistaler and D. Pfenniger

Geneva Observatory, University of Geneva, Sauverny, Switzerland

Preprint online version: April 27, 2020

## ABSTRACT

**Context.** The observation of various ices in cold molecular clouds, the existence of ubiquitous sub-stellar cold  $\text{H}_2$  globules in planetary nebulae and supernova remnants, or the mere existence of comets suggest that the physics of very cold interstellar gas might be much richer than usually envisioned. At the extreme of low temperatures ( $\lesssim 10$  K),  $\text{H}_2$  itself is subject to a phase transition crossing all the cosmic gas density scale.

**Aims.** This well-known laboratory-based fact motivates to study the ideal case of a cold neutral gaseous medium in interstellar conditions for which the bulk of the mass, instead of trace elements, is subject to a gas-liquid or gas-solid phase transition.

**Methods.** On one hand the equilibrium of such fluids is studied using the virial theorem and linear stability analysis. On the other hand the non-linear dynamics is studied by using computer simulations in order to characterize the expected formation of solid bodies analogous to comets. The simulations are run with a state of the art molecular dynamics code (LAMMPS) using the Lennard-Jones inter-molecular potential. The long-range gravitational forces can be taken into account together with short-range molecular forces with finite limited computational resources, by using super-molecules, provided the right scaling is followed.

**Results.** The concept of super-molecule where the phase transition conditions are made independent of the particle mass is tested with computer simulations, allowing to correctly satisfy the ideal gas Jeans instability criterion for one-phase fluids. The simulations show that fluids presenting a phase transition are gravitationally unstable as well, independent of the strength of the gravitational potential, producing two distinct kinds of sub-stellar bodies, those dominated by gravity (“planetoids”) and those dominated by molecular attractive force (“comets”).

**Conclusions.** Observations, formal analysis and computer simulations suggest the possibility of the formation of sub-stellar  $\text{H}_2$  clumps in cold molecular clouds due to the combination of phase transition and gravity. Fluids presenting a phase transition are gravitationally unstable, independent of the strength of the gravitational potential. Arbitrarily small  $\text{H}_2$  clumps may form even at relatively high temperatures, up to 400 – 600 K according to virial analysis. The combination of phase transition and gravity may be relevant for a wider range of astrophysical situations, such as proto-planetary disks.

**Key words.** Instabilities – ISM: clouds – ISM: kinematics and dynamics – ISM: molecules – Methods: analytical – Methods: numerical

## 1. Introduction

### 1.1. Motivation

Typically around 50% or more of the gas in spiral galaxies consists of  $\text{H}_2$ , inferred indirectly by CO or dust emission. Since the discovery of dark molecular hydrogen (Grenier et al. 2005; Langer et al. 2010; Planck Collaboration et al. 2011; Paradis et al. 2012) the estimated quantity of  $\text{H}_2$  in the Milky Way has been essentially doubled, effectively revealing the nature of some of the dark baryons. It is commonly admitted that the CO-related molecular hydrogen is present in relatively dense regions of the interstellar medium, molecular clouds with number density  $> 10^{10} \text{ m}^{-3}$  and temperatures of 7–30 K (Draine 2011).

Even though  $\text{H}_2$  is by far the most abundant molecule ( $\sim 90\%$ ), molecular clouds are mainly detected by CO emissions, due to all the difficulties to detect cold  $\text{H}_2$  (Bolatto et al. 2013), for example  $\text{H}_2$  only starts emitting at temperatures  $> 512$  K. See Combes & Pfenninger (1997) for a review of several possibilities to detect cold  $\text{H}_2$ . Due to the detection difficulties, the real quantity of  $\text{H}_2$  (and He which shares similar properties of discreteness with  $\text{H}_2$ ) in molecular clouds is still rather unknown, especially when its temperature is below  $\lesssim 8$  K down to the Cosmic Background temperature of 2.76 K.

The condensation properties of  $\text{H}_2$  relevant for molecular cloud conditions are well known from laboratory data (Air Liquide 1976). The phase diagram (Fig. 1) shows the domain of pressure conventionally attributed to molecular clouds. But since molecular clouds are highly structured (Pfenninger & Combes 1994), on the way to form here and there eventually stars, one has to keep in mind that large fluctuations in density and temperature must occur since these clouds are commonly observed in a state of supersonic turbulence (Elmegreen & Scalo 2004).

The presence of ice in the interstellar medium consisting of heavier molecules such as  $\text{H}_2\text{O}$ , CO,  $\text{CO}_2$  and  $\text{NH}_3$  covering dust grains is nowadays well documented (Allamandola et al. 1999). Figure 2 shows the location of the critical and triple points of abundant molecules existing in the ISM.  $\text{H}_2$  ice has been detected in absorption band at  $2.417 \mu\text{m}$  (Sandford & Allamandola 1993; Buch & Devlin 1994; Dissly et al. 1994), but the interpretation of such detection is that  $\text{H}_2$  is mixed in  $\text{H}_2\text{O}$ -rich grains in conditions too warm to allow the bulk of  $\text{H}_2$  to condense (Kristensen et al. 2011).

High resolution pictures of nearby planetary nebulae or remnants of supernova have shown the presence of sub-stellar fragments (Walsh & Meaburn 1993). These very cold globules, or knots, each of the size of a few tens of AU, are at least as cold as molecular clouds in the inner parts ( $\sim 10$  K), but much smaller.

An important feature is that the apparent column density in these knots increases inward as long as the resolution allows, or the knot is optically thin (Burkert & O'dell 1998). If these trends extends to the center one can expect there much higher density at colder conditions, which would be ideal to eventually reach a regime where  $H_2$  could condense in liquid or solid form, especially because at high column density the medium blocks not only UV radiation but also cosmic ray heating.

At the level of molecular clouds, even though their *average* properties are well separated from the  $H_2$  phase transition, these are only static properties ignoring the highly dynamical nature of supersonic turbulence observed in the interstellar medium, where fluctuations must be large. Lower temperatures can be reached simply by fast adiabatic decompression. An example of fast decompression is displayed in the Boomerang Nebula which reaches a temperature of only 1 K due to a fast expanding wind (Sahai & Nyman 1997). Thus one should expect, to be coherent with supersonic turbulence, that regions of expansion and compression must be common in the ISM.

The fragmentation of self-gravitating gas leading to collapse has been studied for over a century. The molecular cloud is normally represented as a self-gravitating one-phase fluid (i.e. pure gas), which is governed by the balance between the gravity and the gas pressure. The gravity of this fluid is directly proportional to its density, the pressure to the adiabatic density derivative of the pressure,  $(\partial P / \partial \rho)_s$ . It has been shown by Jeans (1902) that if a perturbation with a long enough wavelength is introduced into the system, this perturbation will grow exponentially. With growing perturbation, the pressure of the fluid will not be able to withstand its gravity anymore, which will ultimately lead to gravitational collapse.

The approximation of molecular clouds as a one-phase fluid is valid in many cases, but when considering very cold, high-density regions, it is an over-simplification. In these condition,  $H_2$  will start creating ice, which has to be taken into account (Walker 2013). The dynamics of such a fluid presenting a phase transition is different from a one-phase fluid, the most important difference being a very low value of  $(\partial P / \partial \rho)_s$  (Johnston 2014). But, as  $(\partial P / \partial \rho)_s$  is crucial for the stability of a fluid, a cold high-density fluid presenting a phase transition is therefore expected to be very unstable.

Based on the observation of sub-stellar globules in planetary nebulas and the dynamics of fluids presenting a phase transition, we may expect the presence of small, sub-stellar  $H_2$  ice-fragments in molecular clouds due to the fragmentation of cold high-density regions. It is of great astronomical interest to study the nature of this sub-stellar fragmentation, as the resulting bound objects may be too small to start nuclear fusion and, thanks to their very low temperature, be very difficult to detect. Some of the baryonic dark matter may actually consist of such fragments (Pfenniger & Combes 1994; Pfenniger et al. 1994).

## 1.2. Approach

In this article, the physics of a self-gravitating van der Waals fluid presenting a phase transition is studied analytically and by simulations. In the analytic part (Sect. 2), the physics of a van der Waals fluid and the related Lennard-Jones (thereafter LJ) potential are recalled. The virial theorem taking into account both the gravitational and the LJ potential is calculated. Its analysis helps to characterize different types of fluids. The stability of a self-gravitating van der Waals fluid presenting a phase transition is then analyzed.

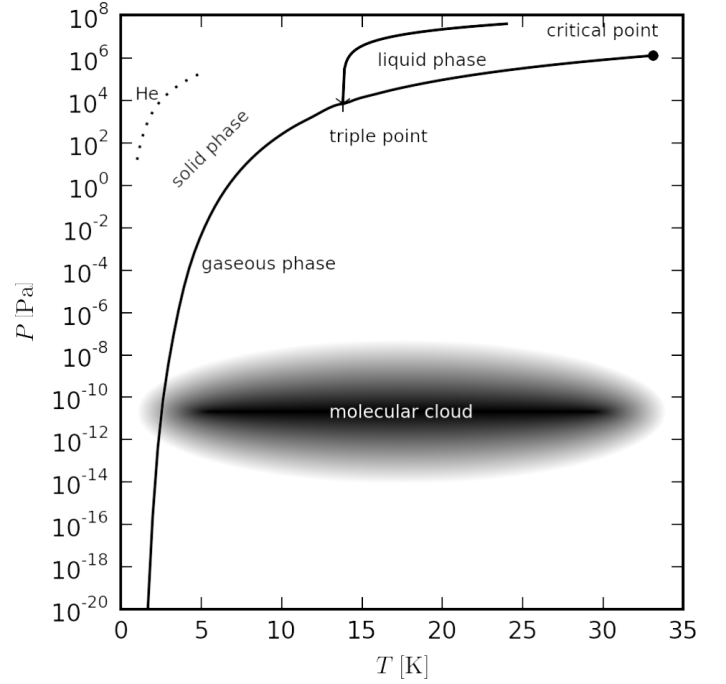


**Fig. 1.**  $H_2$  phase diagram (bold line) and He (dotted line) in cold and low pressure conditions.

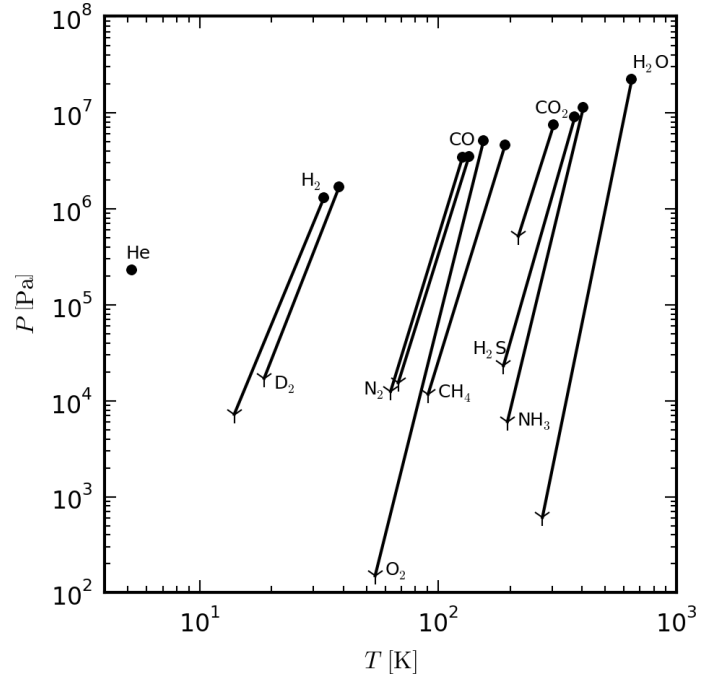


**Fig. 2.** Critical points (bullet) and triple points (v) of common molecules in the ISM. Like for  $H_2$  in Fig. 1, the sublimation curves cross interstellar pressure conditions very steeply in pressure a few K below their triple point. For example, CO should essentially be frozen below  $\sim 20$  K, so unable to emit rotation lines.

In Sect. 3, the molecular dynamics simulator LAMMPS (Plimpton 1995) is introduced. By proper scaling of physical constants the Coulomb force solver is used to calculate the gravitational force, and the short rang molecular force is calculated by using, for the sake of simplicity, the LJ force. In order to be able to perform simulations with a total mass high enough for

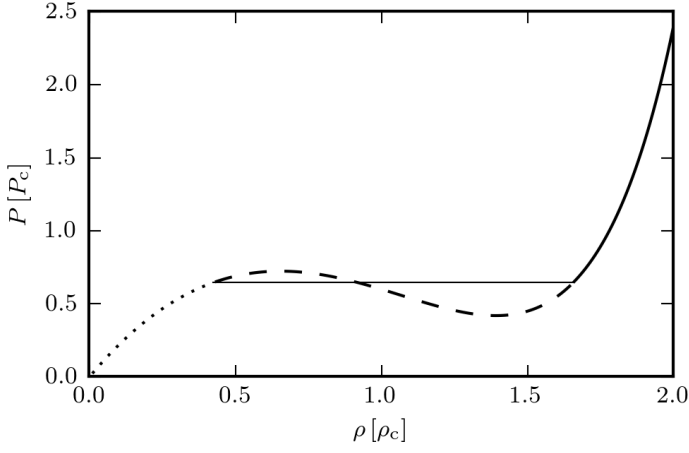


**Fig. 3.** van der Waals phase diagram for a fluid with  $T_r = 0.9$ . Dotted line: gas phase; dashed line: phase transition; solid line: solid phase.

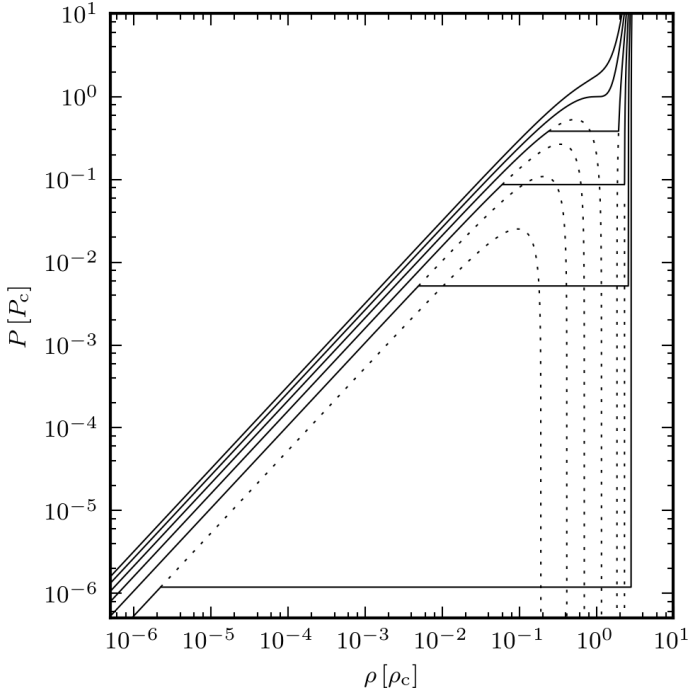


**Fig. 4.** van der Waals phase diagram for a fluid with temperature (from bottom to top) of  $T_r = 0.2$ ,  $T_r = 0.4$ ,  $T_r = 0.6$ ,  $T_r = 0.8$ ,  $T_r = 1.0$  and  $T_r = 1.2$ . Solid line: van der Waals EOS with Maxwell construct, dotted line: original van der Waals EOS.

the fluid to be self-gravitating, the concept of super-molecules is introduced.

The simulations performed are discussed in Sect. 4. First, the correctness of the super-molecule approach is tested. Second, one-phase fluids (i.e., pure gas) are used to test the Jeans criterion. Third, simulations close to a phase transitions are performed, studying the properties of non-gravitating fluids and fluids with a gravitational potential above and below the Jeans criterion.

## 2. Physics of a Fluid presenting a Phase Transition

In this section the physics of a self-gravitating fluid presenting a phase transition is described.

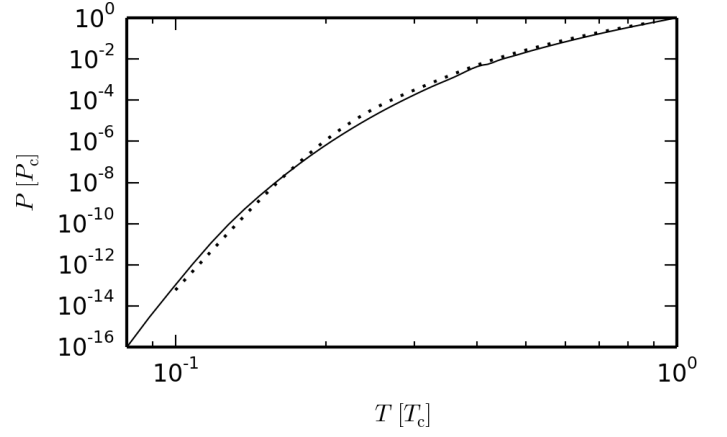


**Fig. 5.** H<sub>2</sub> and van der Waals phase diagrams. Solid line: H<sub>2</sub> laboratory data; dotted line: van der Waals vapor curve derived with the Maxwell construct.

### 2.1. van der Waals Equation

A classical equation of state (EOS) of a pure fluid presenting a first order phase transition is the van der Waals one. This EOS describes the macroscopic behavior of a fluid in which at microscopic level the molecules are strongly repulsive at short distances and beyond that weakly attractive over a limited range.

The van der Waals equation (van der Waals 1910; Johnston 2014) is a modification of the ideal gas law, taking into account the finite size of molecules and the intermolecular interactions. It links pressure, density and temperature as follows:

$$P = \frac{k_B T n}{1 - bn} - an^2 \quad (1)$$

with  $a$  [Pa m<sup>6</sup>] and  $b$  [m<sup>3</sup>] being constants characteristic of the fluid. It can also be expressed in reduced, dimensionless form:

$$P_r = \frac{8T_r}{\frac{3}{n_r} - 1} - 3n_r^2 \quad (2)$$

where  $P_r = P/P_c$ ,  $n_r = n/n_c$  and  $T_r = T/T_c$ .  $P_c$ ,  $T_c$  and  $n_c$  are the values of the thermodynamic critical point (Kondepudi & Prigogine 1998; Carey 1999).

Figure 3 shows the phase diagram for a fluid with  $T = 0.9T_c$ . One can distinguish the gaseous phase (dotted line) and the solid phase (solid line). In-between (dashed line), the fluid presents a phase transition. There are states where  $(\partial P/\partial \rho)_s < 0$ , which is thermodynamically unstable. The parts of the dashed curve where  $(\partial P/\partial \rho)_s > 0$  are metastable for the reason that a lower entropy state is reached when the fluid splits in condensed and gaseous components. The fraction of condensed over gaseous phase grows from 0 to 1 from left to right.

When the two phases coexist the van der Waals EOS is replaced by a constant pressure marked by an horizontal line. This constant pressure level is determined by the Maxwell “equal area” construct (Clerk-Maxwell 1875) demanding a total zero  $P \cdot v$  work for an adiabatic cycle between the fully gaseous to the fully condensed state.

Figure 4 shows the phase diagrams for fluids with temperature from  $T = 0.2T_c$  to  $T = 1.2T_c$ . The dotted line shows the original van der Waals EOS whereas the solid line displays the modified law using the Maxwell construct. There is no Maxwell construct for  $T \geq T_c$  as  $(\partial P/\partial \rho)_s$  is always  $\geq 0$ . Lekner (1982) provides a parametric solution to the van der Waals and Maxwell construct, using  $\Delta s$  as variable.

It is interesting to note that the phase equilibrium pressure is almost identical with the coexistence curve of laboratory data for  $H_2$  over a wide range of pressure (Fig. 5).

### 2.1.1. Lennard-Jones Forces

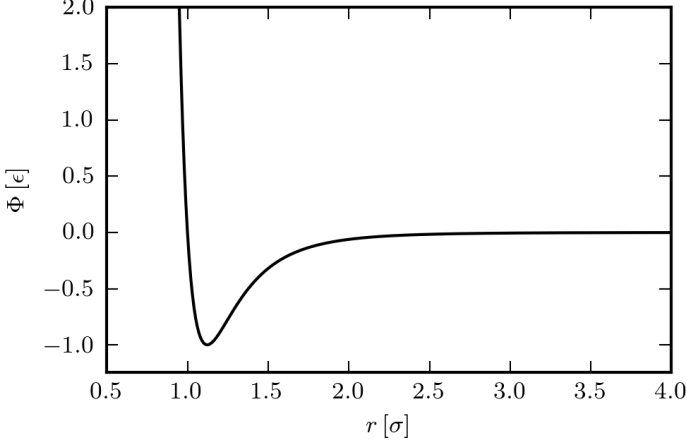


**Fig. 6.** Lennard-Jones potential.

The van der Waals model of phase transition fluid is convenient for a continuum fluid description, but fails to represent the phenomena around the phase transition, which is the reason for correcting it with the above mentioned Maxwell construct. But even with the Maxwell construct, a local thermal equilibrium is still supposed to hold. In astrophysical contexts, often even these assumptions cannot be granted. For instance, in supersonic turbulent situations, ubiquitous in the interstellar medium, thermal equilibrium cannot be satisfied since mechanical energy propagates faster than thermal energy through pressure. Thus any method using quantities like temperature or pressure implicitly assumes that a local thermal equilibrium is established, which makes their use in the supersonic turbulent regime uncertain.

A much less demanding model of fluid is provided by molecular dynamics, where the simplest molecule interactions close to the van der Waals model in equilibrium situations is provided by the Lennard-Jones (LJ) intermolecular potential (Jones 1924). No local or global thermal equilibrium is required. The LJ potential consists of an attractive long-range term and a repulsive short-range term (Fig. 6):

$$\Phi_{LJ}(r) = 4 \frac{\epsilon}{m} \left( r_{\sigma}^{-12} - r_{\sigma}^{-6} \right) \quad (3)$$

with  $r_{\sigma} = r/\sigma$ . Its minimum value, located at  $r_{\sigma} = 2^{1/6}$ , is  $-\epsilon/m$ .

## 2.2. Virial Theorem for a Lennard-Jones gravitating fluid

### 2.2.1. Lagrange-Jacobi Identity

The Virial theorem (Clausius 1870) describes the statistical equilibrium of a system of interacting particles or fluid systems, relating the kinetic and potential energies. In the case of a self-gravitating LJ fluid the LJ potential and gravity combine as a total potential  $\Phi = \Phi_G + \Phi_{LJ}$ .

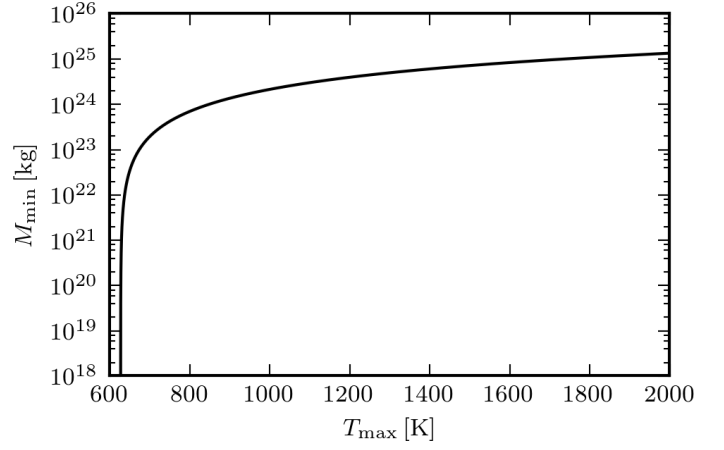


**Fig. 7.** Minimum mass of isothermal equilibrium curves for  $H_2$  homogeneous spheres.

The Virial theorem for this new potential can be derived using the Lagrange-Jacobi identity path, by taking the second time derivative of the moment of the polar inertia  $I \equiv \sum_i m_i r_i^2$ :

$$\frac{1}{2} \frac{d^2 I}{dt^2} = \sum_i m_i \dot{r}_i^2 + \sum_i m_i \mathbf{r}_i \cdot \ddot{\mathbf{r}}_i \quad (4)$$

where the first right-hand term is twice the kinetic energy  $E_{kin}$ , and the second one the virial term. For a system near a statistical equilibrium both sides of this equation should oscillate around 0, so the respective time-averages should vanish.

One notices that the LJ potential is a sum of two homogeneous functions  $^1 \Phi_{LJ} = \Phi_{LJ,a} + \Phi_{LJ,r}$  of degree  $-6$  and  $-12$  respectively, while gravity is of degree  $-1$ . So we can use Euler's theorem of homogeneous functions to express the virial term as a sum of potential energies multiplied by minus the homogeneous degree. The Lagrange-Jacobi identity becomes

$$\frac{1}{2} \frac{d^2 I}{dt^2} = \underbrace{2E_{kin}}_{>0} + \underbrace{12E_{pot,LJ,r}}_{>0} + \underbrace{6E_{pot,LJ,a}}_{<0} + \underbrace{E_{pot,G}}_{<0} . \quad (5)$$

### 2.2.2. Homogeneous Sphere

For homogeneous, finite mass spheres at a given temperature, the individual terms of the Lagrange-Jacobi identity read:

$$2E_{kin} = \frac{3k_B T}{m} M , \quad (6)$$

$$12E_{pot,LJ,r} = 12c_r \frac{\epsilon \sigma^{12} \rho^4}{m^5} M , \quad (7)$$

$$6E_{pot,LJ,a} = -6c_a \frac{\epsilon \sigma^6 \rho^2}{m^3} M , \quad (8)$$

$$E_{pot,G} = -G \left( \frac{36\pi\rho}{125} \right)^{1/3} M^{5/3} , \quad (9)$$

where the constants  $c_r$  and  $c_a$  in the LJ terms have been calculated by straight summation over the  $1.5 \cdot 10^{12}$  nearest molecules, as given in Table 1 for both the simple cubic (SC) and hexagonal close packed (HCP) or face-centered cubic (FCC) lattices.

The virial equation, setting in the Lagrange-Jacobi identity  $d^2 I/dt^2 = 0$ , contain terms proportional to  $M$  except the gravity

<sup>1</sup> By definition, a homogeneous function  $f$  of degree  $k$  satisfies  $f(\lambda \mathbf{x}) = \lambda^k f(\mathbf{x})$ .

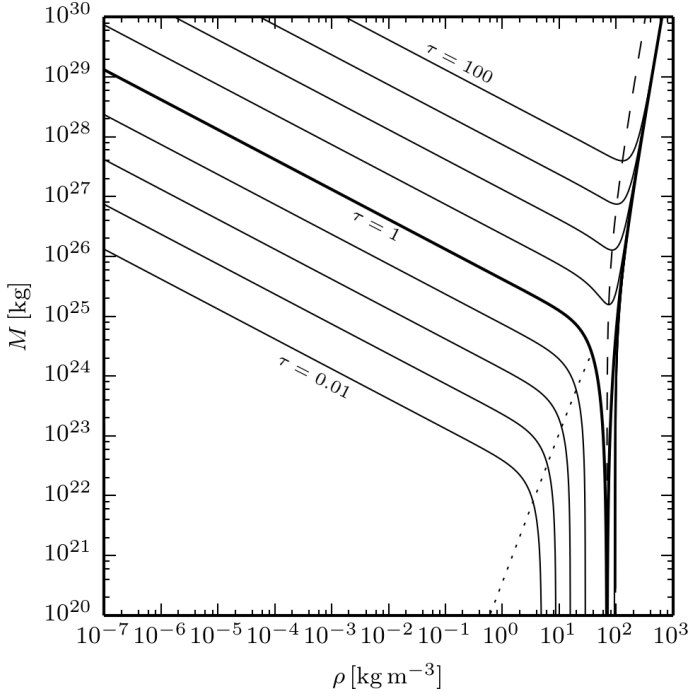


**Fig. 8.** Virial equilibrium of gravitating LJ homogeneous isothermal spheres with  $\text{H}_2$  molecules arranged on a HCP/FCC lattice. The sphere mass as a function of density is plotted for temperatures ranging from  $\tau \equiv T/T_{\text{max}} = 10^{-2}$  to  $10^2$ .

**Table 1.** Lattice constants.

Lattice	$c_r$	$c_a$
SC	24.8085962	33.6076959
HCP/FCC	48.5275208	57.8156842

term which is proportional to  $M^{5/3}$ . Dividing the equation by  $M$  we can separate  $M^{2/3}$ , yielding

$$M^{2/3} = \left(\frac{375}{4\pi\rho}\right)^{1/3} \frac{1}{Gm} \left[ k_B T + 4c_r \epsilon \left(\frac{\sigma^3 \rho}{m}\right)^4 - 2c_a \epsilon \left(\frac{\sigma^3 \rho}{m}\right)^2 \right], \quad (10)$$

which is indeed positive if the terms inside the brackets are also together positive. However the term proportional to  $c_a$  is negative, and when large introduces the possibility that no positive solution for  $M^{2/3}$  exists. Solving the bracket terms equal to zero for  $(\sigma^3 \rho/m)^2$ , we have then a quadratic equation for this term which gives the solutions for the densities  $\rho_0$  for which  $M$  vanishes,

$$\left(\frac{\sigma^3 \rho_0}{m}\right)^2 = \frac{1 \pm \sqrt{1 - 4 \frac{c_r}{c_a^2} \frac{k_B T}{\epsilon}}}{4 \frac{c_r}{c_a}}. \quad (11)$$

The + and – solutions are real non-negative when the term inside the square root above is non-negative. The maximum temperature at which  $M$  can vanish is thus

$$\frac{k_B T_{\text{max}}}{\epsilon} = \frac{c_a^2}{4c_r}. \quad (12)$$

Since the critical temperature for a phase transition in the absence of gravity is about  $\epsilon/k_B$ , we see that  $T_{\text{max}}$  can be substantially larger than the critical temperature. With the values given

in Table 1 for the constants  $c_a$  and  $c_r$ , the maximum temperature below which gravity combined with molecular forces enhances fragmentation are respectively  $T_{\text{max}} = 414.3$  K and 626.8 K for the SC and HCP/FCC lattices, which are 11.38 and 17.22 larger than  $\epsilon/k_B$ .

The corresponding density  $\rho_f$  at which fragmentation can occur at arbitrarily low mass is

$$\rho_f = \frac{m}{\sigma^3} \sqrt{\frac{c_a}{4c_r}}, \quad (13)$$

so of the order of the individual molecule density  $m/\sigma^3$ .

The Lagrange-Jacobi identity therefore allows us to predict a density  $\rho_f$  and a maximum temperature  $T_{\text{max}}$  below which a homogeneous sphere made of LJ molecules can find a gravitational equilibrium at arbitrarily low mass: in a way this provides a simple model, an explanation, for the reason of forming sub-stellar ice clumps out of a cold self-gravitating gas. For  $\text{H}_2$  molecules arranged as SC or HCP/FCC lattice we find  $\rho_f = 73.8 \text{ kg m}^{-3}$  and  $69.2 \text{ kg m}^{-3}$  respectively. These densities are of the order or slightly below the solid or liquid  $\text{H}_2$  density ( $\approx 80 \text{ kg m}^{-3}$ ).

At temperatures  $T > T_{\text{max}}$  the isothermal equilibrium curves have a minimum mass when  $dM/d\rho|_T = 0$ , which is expressed as

$$M_{\text{min}}^2 = K \frac{\epsilon^3 \sigma^3}{G^3 m^4} \frac{c_a^{11/2}}{c_r^{5/2}} \frac{\left[\frac{11}{5}\tau - \left(1 + \sqrt{1 + \frac{11}{25}\tau}\right)\right]^3}{\sqrt{1 + \sqrt{1 + \frac{11}{25}\tau}}}, \quad (14)$$

where  $\tau = T/T_{\text{max}}$  and

$$K = \frac{81}{2\pi} \left(\frac{5}{11}\right)^{11/2} \approx 0.1686476934. \quad (15)$$

Figure 7 shows the minimum mass as a function of the temperature for HCP/FCC  $\text{H}_2$  homogeneous spheres. It is rising very steeply at  $T \gtrsim 627$  K but rising much slower after  $\sim 1000$  K. Interestingly the mass range includes all the masses below terrestrial planet masses for temperatures below  $\text{H}_2$  dissociation.

### 2.2.3. Condensed Bodies

Different condensed and uncondensed bodies can be identified using the Lagrange-Jacobi identity, as summarized in Table 2.

**Table 2.** Condensed and uncondensed bodies in a LJ fluid using the Lagrange-Jacobi identity.

Dominating Terms	Name
$2E_{\text{kin}} + 6E_{\text{pot,LJ,a}}$	“molecular gas”
$12E_{\text{pot,LJ,r}} + 6E_{\text{pot,LJ,a}}$	“comet”
$12E_{\text{pot,LJ,r}} + E_{\text{pot,G}}$	“rocky planetoid”
$2E_{\text{kin}} + E_{\text{pot,G}}$	“gaseous planetoid”

Figure 8 shows some  $M(\rho, T)$  equilibrium curves of gravitating homogeneous sphere whose molecules are arranged on a HCP/FCC lattice, which is able to represent the most compact sphere lattice at high density. At low density, on the left of the diagram, the equilibrium is fixed by principally the attractive part of molecules and their temperature and the exact lattice structure is irrelevant, this is the domain of uncondensed “molecular gas”.

On the right there is an accumulation curve around  $\rho \approx 100 \text{ kg m}^{-3}$  representing purely condensed  $\text{H}_2$  bodies mainly balancing gravity with the repulsive part of molecules. The area between the dashed line, connecting the minimum of the isotherms with  $T > T_{\text{max}}$ , and the accumulation curve is the domain of the “rocky planetoids”.

At temperatures below  $T_{\text{max}} = 626.8 \text{ K}$  the equilibrium curves do plunge to arbitrarily low masses along two regimes, the left vertical asymptotes represent the limit gaseous bodies, and the right asymptotes the condensed (solid or liquid) bodies, called “comets”. The area of the “comets” lies between the dotted line, connecting the elbows of the isotherms with  $T < T_{\text{max}}$ , and the dashed line.

At high temperature and low density, left of both the dotted and dashed line, and above the isotherm lines, lie the “gaseous planetoids”. These bodies’ equilibrium is fixed principally by gravity and temperature.

Of course real astrophysical bodies are not homogeneous, in practice in the low mass regime one can expect bodies made of a mixture of condensed state in the core surrounded by a less dense gaseous atmosphere, which could be calculated by solving the hydrostatic equilibrium (see Pfenniger (2004) where some models of isothermal bodies made of  $\text{H}_2$  containing a solid core and a gaseous atmosphere have been discussed).

### 2.3. Gravitational Instability

The linearized wave equation for the isentropic density perturbation  $\rho_{\text{per}}$  of a self-gravitating fluid of density  $\rho$  is (Jeans 1902; Weinberg 1972):

$$\frac{\partial^2 \rho_{\text{per}}}{\partial t^2} - \left( \frac{\partial P}{\partial \rho} \right)_s \nabla^2 \rho_{\text{per}} = 4\pi G \rho \rho_{\text{per}}. \quad (16)$$

Its solution is a superposition of modes of the form  $\exp(i(\mathbf{k} \cdot \mathbf{x} - \omega t))$  with  $\omega$  the frequency and  $k = 2\pi/\lambda$  the wavenumber, where  $\lambda$  is the wavelength. This leads to the instability condition (Jeans 1902)

$$\omega^2 = \left( \frac{\partial P}{\partial \rho} \right)_s k^2 - 4\pi G \rho < 0. \quad (17)$$

When fulfilled the modes are real-exponential, therefore unstable. The classical Jeans criterion reads:

$$\lambda > \lambda_J \equiv \sqrt{\left( \frac{\partial P}{\partial \rho} \right)_s \frac{\pi}{G \rho}}. \quad (18)$$

Therefore the effective gravitational instability is directly dependent on the EOS of the medium.

#### 2.3.1. Ideal Gas

In most textbooks about Jeans instability only the ideal gas is discussed. In the case of an ideal monoatomic gas, the pressure derivative term is:

$$\left( \frac{\partial P}{\partial \rho} \right)_s = \gamma \frac{k_B T}{m} \quad (19)$$

with the adiabatic index  $\gamma = 5/3$ . This value is always positive which leads to the classical, ideal monoatomic gas Jeans criterion for instability:

$$\lambda > \lambda_J = \sqrt{\frac{\pi \gamma k_B T}{G \rho m}}. \quad (20)$$

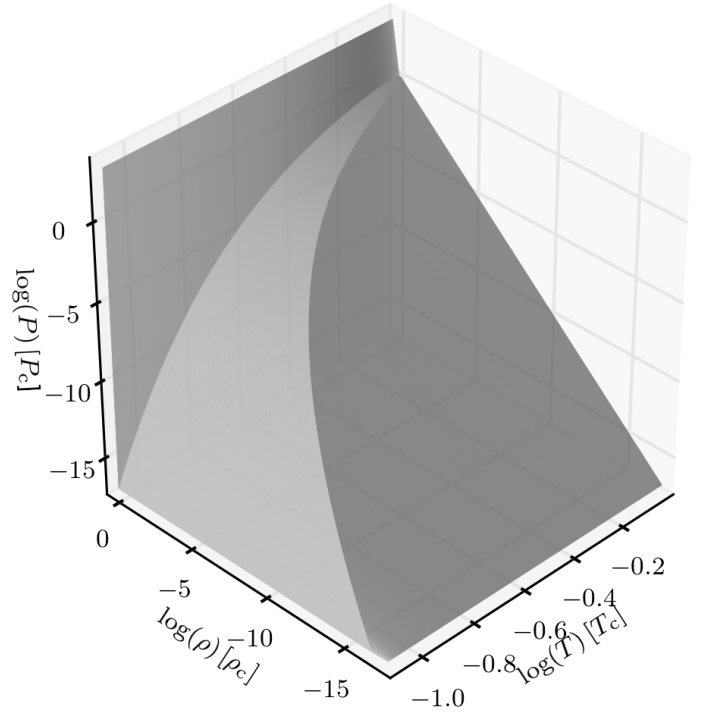


**Fig. 9.** van der Waals EOS including the Maxwell construct.

#### 2.3.2. Fluid with Phase Transition

When considering a fluid presenting a phase transition the term  $(\partial P / \partial \rho)_s$  may differ from the one of an ideal gas. As seen before, in the case of the van der Waals EOS, the Maxwell construct must be used, which may change considerably the combined stability of the fluid (Sect. 2.1). In the presence of a phase transition, the EOS gradient is strongly modified, in particular  $(\partial P / \partial \rho)_T = 0$ . Using

$$\left( \frac{\partial P}{\partial \rho} \right)_s = \frac{c_p}{c_v} \left( \frac{\partial P}{\partial \rho} \right)_T \quad (21)$$

with  $c_p$  and  $c_v$  both finite values, we find  $(\partial P / \partial \rho)_s = 0$ . Therefore, a self-gravitating fluid in a phase transition is also automatically gravitationally unstable.

Figure 9 shows the 3D representation of the EOS including the Maxwell construct. Clearly the curved triangular region, the phase transition region (on the left) has a very different gradient than the almost ideal gas region at low density-high temperature, or the condensed phase region at high density. It is remarkable that a temperature drop by one order of magnitude from the critical temperature leads to a drop in the critical pressure by 14 orders of magnitude. For example for  $\text{H}_2$  at 3 K the critical pressure is  $6.4 \cdot 10^{-9} \text{ Pa}$ .

### 3. Molecular Dynamics

For all simulations, the Large-Scale Atomic/Molecular Massively Parallel Simulator (LAMMPS) is used (Plimpton 1995). LAMMPS is a state of the art and widely used single and multi processor code in chemistry, material sciences and related fields. Its abilities to quickly compute short and long range forces and the possibility to use a multi-timescale integrator make it a suitable tool to perform our simulations.

### 3.1. Potential Solver

LAMMPS has a wide range of force fields. For the simulations in this article we use only the LJ and the self-gravitational potentials.

Since the straight calculation cost for exact pairwise interactions is  $O(N^2)$ , approximate but still accurate methods are implemented which make the calculations possible with much lower cost. LAMMPS uses a cut-off radius  $r_c$  for the short-range forces. As the attractive part of the LJ potential drops with  $r^{-6}$ , it is calculated only for neighbor particles within  $r_c$ . The neighbors for each particle are found using a Verlet neighbor list. This list is created with a radius of  $r_n = r_c + r_s$ ,  $r_s$  being a extra “skin” distance to avoid the recalculation of the Verlet list at every time-step. This cut-off method is  $O(N)$  and scales therefore linearly with the number of particles.

The gravitational potential drops with  $r^{-1}$  so the long range interactions cannot be ignored. It is calculated using the Particle<sup>3</sup>-Mesh (P<sup>3</sup>M) method (Hockney & Eastwood 1981): The gravitational potential is split in a short-range and a long-range part in Fourier space (Ewald 1921):

$$\hat{\Phi} = \hat{\Phi}_{\text{SR}} (1 - \exp(-k^2 r_s^2)) + \hat{\Phi}_{\text{LR}} \exp(-k^2 r_s^2) \quad (22)$$

where  $r_s$  is the splitting distance.  $\Phi_{\text{SR}}$  is calculated on the same time as the LJ potential using the same Verlet list,  $\Phi_{\text{LR}}$  is calculated in Fourier space using a fast Fourier transform (FFT).

As LAMMPS is designed for the simulation of chemical substances not far from terrestrial conditions, self-gravity is too weak to be of any influence, no specific self-gravity module is provided. For that reason, a tweak is used by using the Coulomb’s potential module for an electric field:

$$\Phi_C = \frac{C q_i q_j}{\epsilon r} \quad (23)$$

where  $C$  is the interaction constant,  $\epsilon$  the dielectric constant and  $q_{i,j}$  the charges of the molecules. As  $C$  is fixed in LAMMPS, to correctly calculate the gravitational potential we set the constants as follows:

$$\epsilon = -1, \quad (24)$$

$$q_i = \sqrt{\frac{G}{C}} m_i. \quad (25)$$

### 3.2. Time Integration

The time integration is done using the symplectic leapfrog scheme. The drift and kick operators,

$$D(\Delta t) \equiv x(t + \Delta t) = x(t) + \Delta t \dot{x}(t), \quad (26)$$

$$K(\Delta t) \equiv \dot{x}(t + \Delta t) = \dot{x}(t) + \Delta t \ddot{x}(t), \quad (27)$$

are applied according to the sequence  $K\left(\frac{\Delta t}{2}\right) D(\Delta t) K\left(\frac{\Delta t}{2}\right)$  at each elementary time-step. For short-range force the time-step is constant throughout the simulation and set as  $10^{-2} - 10^{-3}$  the typical interaction time-scale during nearest-neighbor molecular interactions. This is reasonable since the repulsive interaction and the finite kinetic energy prevent strongly varying accelerations between particles.

Small changes of individual particle positions can significantly change the short-range forces, which is why a very small time-step is required. But such small changes have almost no influence on the long-range forces. For this reason, there is no need to calculate the long-range forces at every time-step.

In regard of the short-range calculations, the long-range calculations are an order of magnitude more costly per step but need always the same amount of calculation time: Creation of the density-map with a fifth order interpolation procedure, a FFT solution of the potential and the same interpolation procedure for finding the accelerations.

With the “reversible reference system propagator algorithm” (rRESPA), a multiple time-scale integrator is available for LAMMPS which enables to reduce the number of long-range force calculation (Tuckerman et al. 1992). It enables time integration in up to 4 hierarchical levels, but only two are needed for the simulations presented in this article. The rRESPA time-integration-scheme looks as follows:

$$K_{\text{LR}}\left(\frac{\Delta t}{2}\right) \left[ K_{\text{SR}}\left(\frac{\Delta t}{2n_{\text{SR}}}\right) D\left(\frac{\Delta t}{n_{\text{SR}}}\right) K_{\text{SR}}\left(\frac{\Delta t}{2n_{\text{SR}}}\right) \right]^{n_{\text{SR}}} K_{\text{LR}}\left(\frac{\Delta t}{2}\right) \quad (28)$$

where  $n_{\text{SR}}$  is the number of short-range iterations and set as 10 – 100,  $K_{\text{LR}}$  is the kick operator using the long-range (FFT) accelerations and  $K_{\text{SR}}$  the kick operator using the short-range accelerations.

### 3.3. Super-Molecules

The maximum number of particles which can be simulated on today’s supercomputers is of the order of  $10^9 - 10^{10}$  particles. But even using such a huge number of molecules would only result in a fluid with a total mass of a few femtograms. It is obvious that gravity has no effect on such a fluid. For that reason, the concept of *super-molecules* is introduced. This concept is well established in galactic dynamics simulation, where *super-stars* weight typically  $10^4 - 10^6 M_\odot$ , and in cosmology where *super-WIMPS* may weight as much as  $\sim 10^{67} \text{ GeV} c^{-2}$  particles. Two-body relaxation or diffusion due to the low number of super-particles is negligible provided the simulation time is not too large depending on the specific problem. Practice has shown that such an approximation is valid in galactic dynamics for instance if the simulation length is of order 100 dynamical times (Binney & Tremaine 2008).

The basic principle of the concept is that each super-molecule consists of  $\eta$  molecules, its mass is therefore:

$$m_{\text{SM}} = \eta m_{\text{M}}. \quad (29)$$

To have the same properties of a super-molecule fluid as for a normal fluid, every term of the virial Equ. (5) has to be transformed such that the ratios of the terms are invariant. The kinetic energy term reads

$$2E_{\text{kin}} = N_{\text{M}} m_{\text{M}} \langle v_{\text{M}}^2 \rangle = N_{\text{SM}} m_{\text{SM}} \langle v_{\text{SM}}^2 \rangle. \quad (30)$$

Since the total mass is constant,  $N_{\text{M}} m_{\text{M}} = N_{\text{SM}} m_{\text{SM}}$ , the velocity dispersion of molecules and super-molecules is also the same

$$\langle v_{\text{SM}}^2 \rangle = \langle v_{\text{M}}^2 \rangle. \quad (31)$$

From the two LJ terms, Equ. (7–8) remain the same if

$$\frac{\epsilon_{\text{M}} \sigma_{\text{M}}^{12}}{m_{\text{M}}^5} = \frac{\epsilon_{\text{SM}} \sigma_{\text{SM}}^{12}}{m_{\text{SM}}^5}, \quad (32)$$

$$\frac{\epsilon_{\text{M}} \sigma_{\text{M}}^6}{m_{\text{M}}^3} = \frac{\epsilon_{\text{SM}} \sigma_{\text{SM}}^6}{m_{\text{SM}}^3}. \quad (33)$$

Solving these two equations and using Equ. (29), we derive

$$\epsilon_{\text{SM}} = \eta \epsilon_{\text{M}}, \quad (34)$$

$$\sigma_{\text{SM}} = \sqrt[3]{\eta} \sigma_{\text{M}}. \quad (35)$$

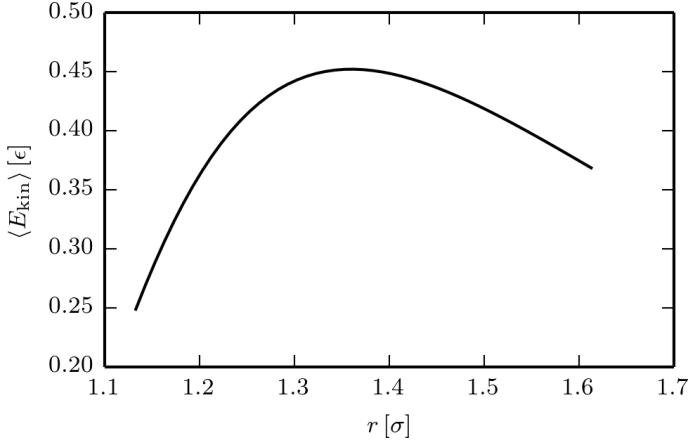


**Fig. 10.** Mean kinetic energy as a function of the maximum displacement in an ice clump.

The gravitational energy Equ. (9) doesn't change since it doesn't depend on super-molecule properties.

It is important to ensure that the gravitational force between two super-molecules remains small compared to the corresponding LJ force within the short-range force cut-off radius. This is assured by setting  $F_G(r_c) \ll F_{\text{LJ}}(r_c)$  with  $r_c$  being the cut-off radius. This leads to the following constraint:

$$\eta^2 \ll \frac{24\epsilon_M\sigma_M}{Gm_M^2} (r_{c,\text{SM}}^{-5} - 2r_{c,\text{SM}}^{-11}), \quad (36)$$

where  $r_{c,\text{SM}} = (r_c/\sigma_{\text{SM}})$ . Using a cut-off radius of  $r_c = 4\sigma$  and hydrogen super-molecules, we find a maximum super-molecule mass equal to  $5.7 \cdot 10^{-6} M_\oplus$ , meaning at least  $1.7 \cdot 10^5$  particles are required for simulating an Earth mass virialized  $\text{H}_2$ -condensed body.

### 3.4. Ice Clump Detection

The LJ potential has its minimum at  $r_m = 2^{1/6}\sigma$ . If an ice clump is at absolute zero temperature, all bound molecules would have this distance from at least one other molecule. But, as the molecules in a clump are vibrating, the maximum binding distance between two molecules is generally larger than  $r_m$ .

The simplest clump consists of two molecules. Their mean kinetic energy as a function of the maximum displacement can be calculated numerically (Fig. 10).

The mean kinetic energy rises up to the maximum value of  $r_{\sigma,\text{max}} = 1.3625$ , after which it drops again. It can be assumed that all stable clumps have a binding distance below this value. The distance constraint for two molecules to be bound is therefore:

$$r_\sigma \leq r_{\sigma,\text{max}} \quad (37)$$

Using  $r_{\sigma,\text{max}}$  as the threshold distance, LAMMPS provides a list of clumps at fixed time intervals.

## 4. Simulations

### 4.1. Units

A fluid is defined by the number of super-molecules  $N_{\text{SM}}$ , the initial velocity distribution (temperature), the number density, and the strength of the gravitational potential. All simulation properties are molecule-independent, the initial temperature and density are measured as a factor of the critical values  $T_{\text{cr}}$  and  $n_{\text{cr}}$ , and

**Table 3.** Parameters of the super-molecule test simulations.

Name	$n/n_{\text{cr}}$	$T/T_{\text{cr}}$	$N_{\text{SM}}$
SM15	0.006	1.5	$4^3 - 200^3$
SM30	0.006	3.0	$4^3 - 200^3$
SM60	0.006	6.0	$4^3 - 200^3$
SM04	0.1	0.4	$25^3 - 200^3$
SM06	0.1	0.4	$25^3 - 200^3$
SF <sup>a</sup>	0.1	0.1	$50^3 - 160^3$

**Notes.** All simulations are without gravity and use the basic KDK time integration scheme.

<sup>(a)</sup> External gravity  $a = 0.1 (L/\tau^2)$

**Table 4.** Parameters of the one-phase fluid simulations.

Name	$n/n_{\text{cr}}$	$T/T_{\text{cr}}$	$N_{\text{SM}}$	$\gamma_J$
OP0	$10^{-2}$	1.25	$100^3$	0
OPGw	$10^{-2}$	1.25	$100^3$	0.5
OPGs	$10^{-2}$	1.25	$50^3 - 160^3$	1.25

**Notes.** OP0 without gravity and using the KDK time integration scheme. All gravitational simulations use the P<sup>3</sup>M gravitational solver and the rRESPA time scheme.

**Table 5.** Parameters of the phase transition simulations.

Name	$n/n_{\text{cr}}$	$T/T_{\text{cr}}$	$N_{\text{SM}}$	$\gamma_J$
OPGs	$10^{-2}$	1.25	$50^3 - 160^3$	0, 0.5, 1.25
PT1-1	$10^{-1}$	0.1	$50^3, 100^3$	0, 0.5, $G = G_{\text{OPGs}}$
PT2-1	$10^{-1}$	0.2	$50^3, 100^3$	0, 0.5, $G = G_{\text{OPGs}}$
PT3-1	$10^{-1}$	0.3	$50^3, 100^3$	0, 0.5, $G = G_{\text{OPGs}}$
PT1-2	$10^{-2}$	0.1	$50^3, 100^3$	0, 0.5, $G = G_{\text{OPGs}}$
PT2-2	$10^{-2}$	0.2	$50^3 - 100^3$	0, 0.5, $G = G_{\text{OPGs}}$
PT3-2	$10^{-2}$	0.3	$50^3 - 100^3$	0, 0.5, $G = G_{\text{OPGs}}$
PT5-2	$10^{-2}$	0.5	$50^3, 100^3$	0, 0.5, $G = G_{\text{OPGs}}$
PT7-2	$10^{-2}$	0.7	$50^3, 100^3$	0, 0.5, $G = G_{\text{OPGs}}$
PT9-2	$10^{-2}$	0.9	$50^3, 100^3$	0, 0.5, $G = G_{\text{OPGs}}$
PT1-3	$10^{-3}$	0.1	$50^3, 100^3$	0, 0.5, $G = G_{\text{OPGs}}$
PT2-3	$10^{-3}$	0.2	$50^3, 100^3$	0, 0.5, $G = G_{\text{OPGs}}$
PT3-3	$10^{-3}$	0.3	$50^3, 100^3$	0, 0.5, $G = G_{\text{OPGs}}$

**Notes.** All simulations in two different runs: without gravity and perturbation, using basic KDK time integration scheme, and with gravity and perturbation, using the P<sup>3</sup>M gravitational solver and the rRESPA time scheme.

the gravitational potential is measured as the factor  $\gamma_J = G/G_J$  of the ideal Jeans gravity  $G_J$ , defined as

$$G_J = \frac{\pi\gamma k_B T_0}{nm^2 L^2} \quad (38)$$

with the box side  $L = (N_{\text{SM}}/n)^{1/3}$ . It is interesting to note that  $G_J$  is proportional to temperature and inversely proportional to density. For all simulations, the time unit is defined as the average time of a particle crossing the box:

$$\tau = \frac{L}{V} \quad (39)$$

with  $V^2 = \sum_i v_{x_i}^2/N$ .

The distance at which the gravitational and LJ forces are equal is denoted as

$$x_{\text{GLJ}} \equiv F_G(x_{\text{GLJ}}) = F_{\text{LJ}}(x_{\text{GLJ}}). \quad (40)$$



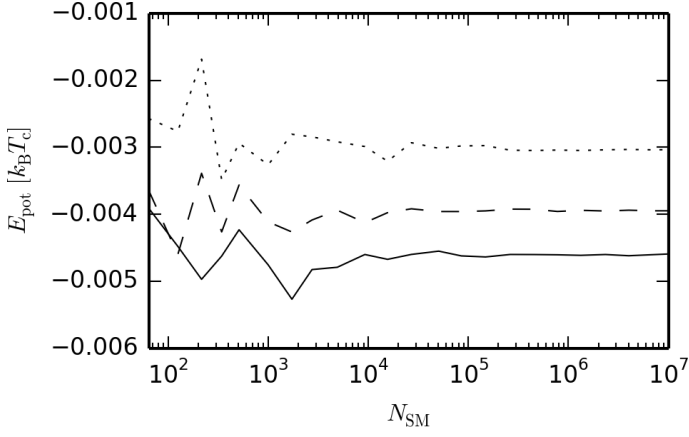


**Fig. 11.** LJ potential energy as a function of the number of super-molecules at  $t = 1\tau$ . Solid line: SM15; dashed line: SM30; dotted line: SM60.

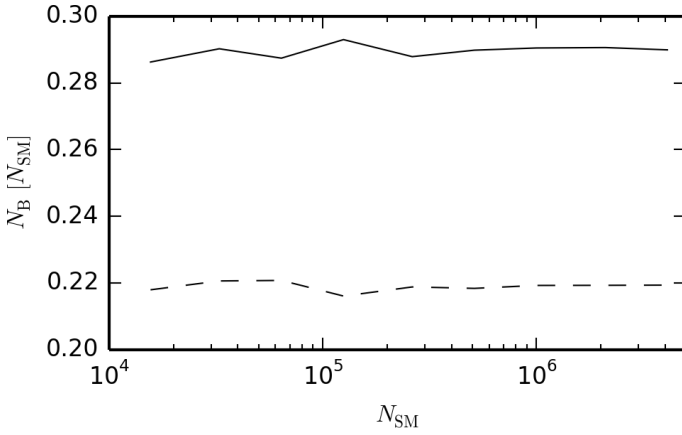


**Fig. 12.** Fraction of bound molecules as a function of the number of super-molecules at  $t = 5\tau$ . Solid line: SM04, dashed line: SM06.

## 4.2. Super-Molecule Concept Tests

### 4.2.1. Potential Energy

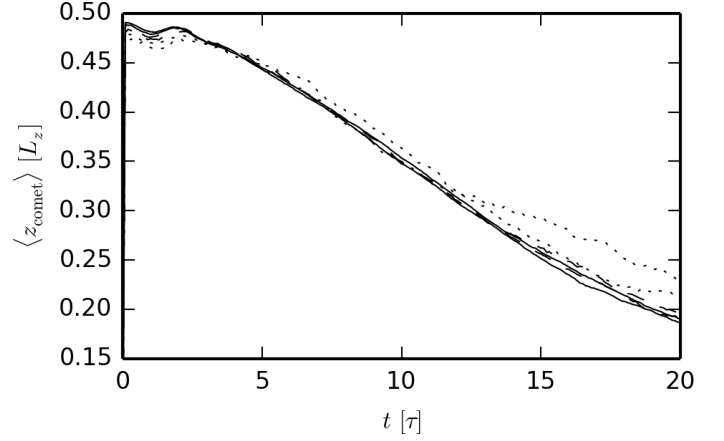
A fluid in a cubic box with periodic boundary conditions and initial constant density of  $n = 0.006 n_{\text{cr}}$  is simulated with LAMMPS. Three different initial Maxwellian velocity distributions with temperature  $T = 1.5, 3.0$  and  $6.0 T_{\text{cr}}$ , and a number of particles from  $N_{\text{SM}} = 30^3 - 200^3$  are used. Table 3 shows the parameters of the different simulations.

Figure 11 shows the LJ potential energy of those three fluids with respect to the number of super-molecules. One can see fluctuations in the simulations with low  $N_{\text{SM}}$ , but the result becomes reasonable when  $N_{\text{SM}} > 10^4$ , and a satisfactory convergence is obtained if  $N_{\text{SM}} > 10^5$ . Therefore all the subsequent simulations are performed with  $N_{\text{SM}} > 10^5$ .

### 4.2.2. Cluster Percentage

High density, low temperature fluids are simulated during  $5\tau$  at various number of super-molecules. These fluids will form “comets” and allow to compare the final percentage of bound molecules. Table 3 shows the parameters of the different simulations.

Figure 12 shows the fraction of bound molecules with respect to the number of super-molecules. All simulations reach



**Fig. 13.**  $z$ -Coordinate of the center of mass of “comets” as a function of time of the SF simulation.  $N_{\text{SM}} = 50^3$  and  $64^3$  (dotted line),  $80^3$  and  $100^3$  (dashed line),  $128^3$  and  $160^3$  (solid line).

the same percentage, independent of the number of super-molecules.

### 4.2.3. Precipitation in an External Field

An external acceleration is applied in the  $-z$  direction to a fluid within a box with reflecting boundary conditions. The fluid is very cold and rather dense (see Table 3) and is therefore forming ice grains, or “comets”. Due to the acceleration and Archimedes’s principle, the “comets” fall to the bottom and stay there, similar to snow fall on Earth.

The purpose of this simulation is to test the time-scaling of the precipitation as function of the number of particles. Figure 13 shows the  $z$ -coordinate of the center of mass of “comets” as a function of time. The curves are very similar, with a slight over-estimation of the fall-time for the smallest simulation. Therefore the precipitation phenomenon timescale is not strongly dependent on the mass resolution.

## 4.3. Fluid with Perturbation

To illustrate the behavior of a homogeneous fluid perturbed by a plane sinusoidal wave, a velocity perturbation in the  $x$  direction is introduced with wavelength  $\lambda$  equal to the box side  $L$ . Starting with a Maxwellian distribution  $v_i$  of velocities for the homogeneous unperturbed case, the  $x$ -component of the velocities is perturbed in such a way as to conserve energy. The perturbed  $x$ -velocity component for each particle  $i$  reads

$$v'_{xi} = \alpha [v_{xi} + \beta V \sin(\omega x_i)] \quad (41)$$

with  $\omega = 2\pi/L$ . The correction factor  $\alpha \leq 1$  is used to keep the same kinetic energy in the  $x$  direction, with

$$\alpha^2 = \frac{\sum_i v_{xi}^2}{\sum_i [v_{xi} + \beta V \sin(\omega x_i)]^2}. \quad (42)$$

$\beta$  determines the strength of the perturbation but is supposed to be small enough to be in the linear regime of perturbations. In the present simulations,  $\beta = 0.01$ .

## 4.4. One-Phase Fluid

To study the reaction of a pure one-phase ideal gas fluid far from the phase transition but with the above plane-wave per-

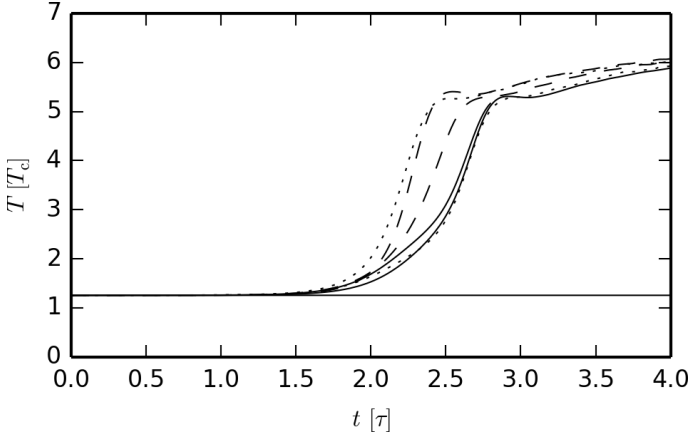


**Fig. 14.** Temperature of the one-phase fluid simulations OP0 (straight solid line) and OPGs as a function of time.  $N_{\text{SM}} = 50^3$  and  $64^3$  (dotted line),  $80^3$  and  $100^3$  (dashed line),  $128^3$  and  $160^3$  (solid line).

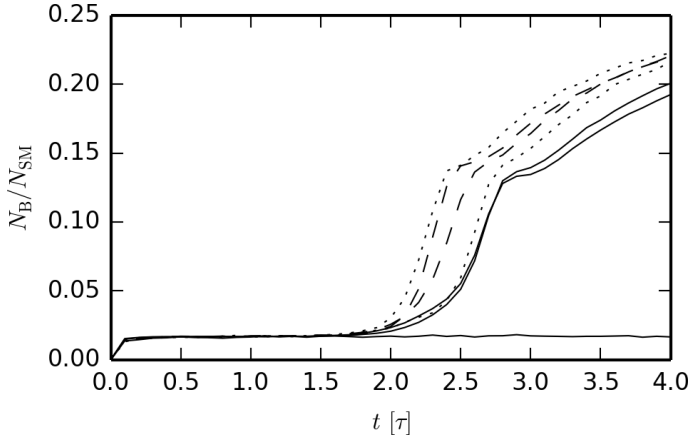


**Fig. 15.** Fraction of bound molecules in “comets” of the one-phase fluids OP0 (straight solid line) and OPGs as a function of time.  $N_{\text{SM}} = 50^3$  and  $64^3$  (dotted line),  $80^3$  and  $100^3$  (dashed line),  $128^3$  and  $160^3$  (solid line).

turbation, the initial temperature is taken above the critical value ( $T_0 = 1.25 T_{\text{cr}}$ ) and the initial density well below the critical value ( $n_0 = 10^{-2} n_{\text{cr}}$ ). Three different cases are studied: without gravity, weakly self-gravitating below the classical ideal gas Jeans criterion with  $\gamma_J = 0.5$ , and sufficiently self-gravitating above the ideal gas Jeans criterion with  $\gamma_J = 1.25$ . The simulations are performed with  $N_{\text{SM}}$  ranging from  $50^3$  to  $160^3$ . Table 4 shows the parameters of the different simulations.

#### 4.4.1. Time Evolution

As the simulations conserve total energy, the formation of “comets” (implying a decrease of potential energy) can be measured by the mean temperature (i.e., kinetic energy) of the system. This is equivalent to the release of latent heat when a gaseous fluid condenses.

Figures 14 and 15 display the temperature and the “comet” percentage evolutions of the one-phase fluid simulations: OP0 without gravity and  $N_{\text{SM}} = 100^3$  super-molecules and the sufficiently self-gravitating fluids OPGs with  $N_{\text{SM}}$  ranging from  $50^3$  to  $160^3$ . The weakly self-gravitating fluid of simulation OPGw is not shown since it is identical to the no gravity case OP0.

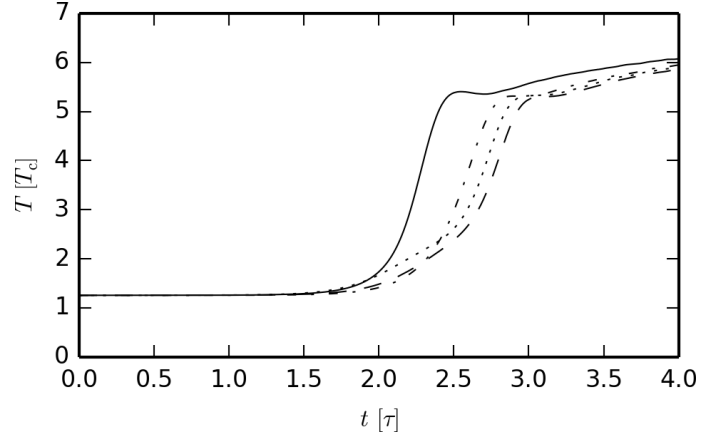


**Fig. 16.** Temperature of the one-phase fluid simulations OPGs as a function of time.  $N_{\text{SM}} = 100^3$  with four different random seeds.

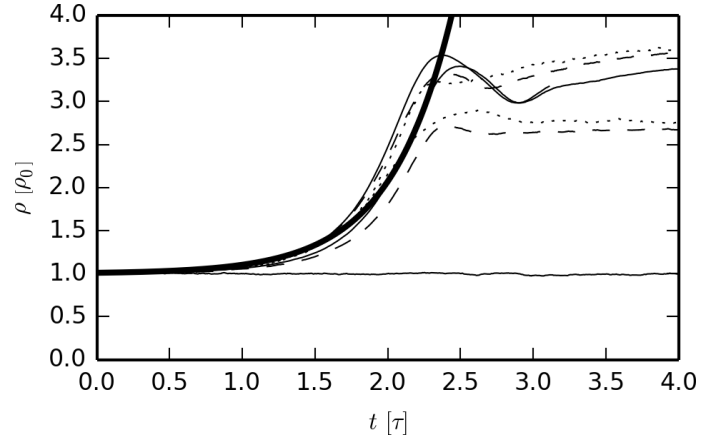


**Fig. 17.** Density at  $x = (0.5 \pm 0.05)L$  of the one-phase fluids OP0 (straight solid line) and OPGs as a function of time. Bold line: analytic solution for ideal gas.  $N_{\text{SM}} = 50^3$  and  $64^3$  (dotted line),  $80^3$  and  $100^3$  (dashed line),  $128^3$  and  $160^3$  (solid line).

For the fluid without gravity OP0 and the weakly self-gravitating fluid OPGw, no particular effect is observed. The percentage of “comets” rises to  $\lesssim 2\%$ , which can be attributed to the initial fluctuations in the distribution. The small perturbation introduced in the  $x$ -direction does not change the nature of the fluid, its temperature and “comet” percentage remains the same.

The sufficiently self-gravitating OPGs fluids on the other hand do change. Their temperatures and cluster percentages are rising steeply showing a substantial latent heat release. All simulations reach the same asymptotic temperature  $\sim 6T_{\text{cr}}$ , but different initial conditions (i.e., random seeds) yield slightly different behaviors during the collapse. This can also be observed in Fig. 16 where four identical parameter simulations but different random seeds are run with  $N_{\text{SM}} = 100^3$ , leading to a time-difference of  $\sim 0.5\tau$  for reaching the asymptotic upper value.

Figure 17 shows the density increase around the center of the perturbation in the range  $x = (0.5 \pm 0.05)L$  and compares them to the analytic solution for an ideal gas. The simulations follow the ideal gas solution with a slight dispersion up to  $t \approx 2.5\tau$ , where a density rise is not possible anymore due to the repulsive LJ force; the density declines for a short while due to the collapse rebound down to a minimum at  $t \approx 2.7\tau$ . This density local minimum

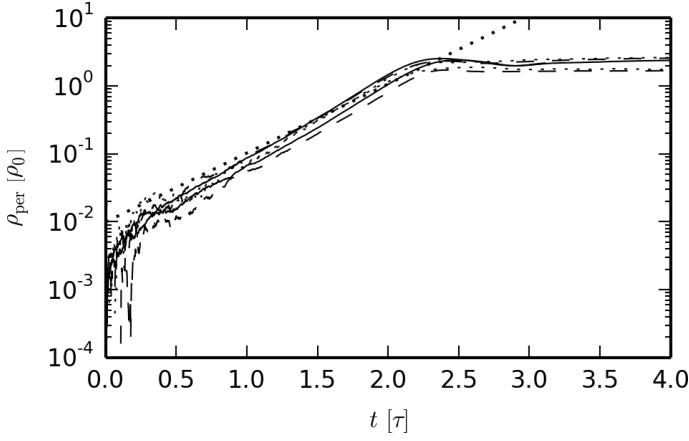


**Fig. 18.** Evolution of perturbation density. Straight dotted line: analytic solution for ideal gas.  $N_{\text{SM}} = 50^3$  and  $64^3$  (dotted line),  $80^3$  and  $100^3$  (dashed line),  $128^3$  and  $160^3$  (solid line).

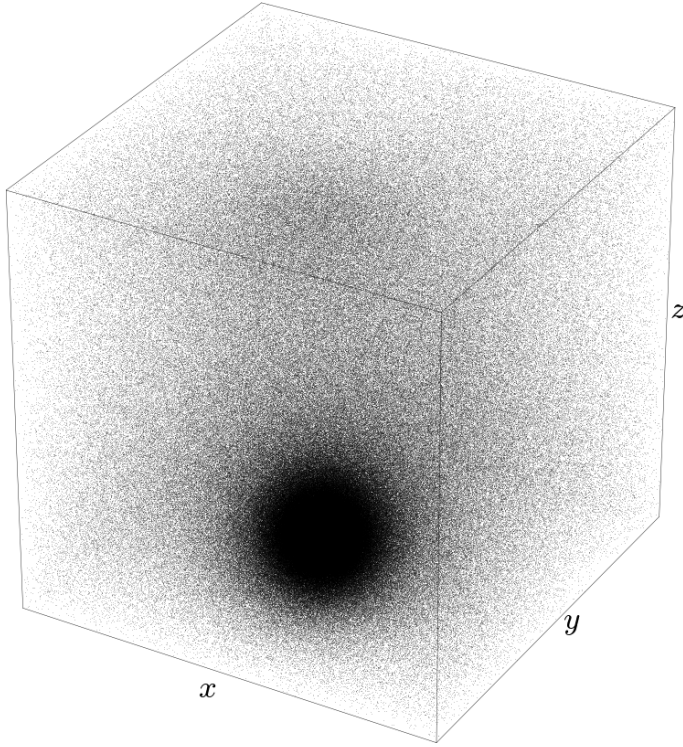


**Fig. 19.** 3D-view of simulation OPGs with  $N_{\text{SM}} = 100^3$  at  $t = 4\tau$ .

corresponds with the break in the temperature increase visible in Fig. 14. Subsequently the temperature growth is much slower.

Figure 18 shows the evolution of density in the simulations, and the predicted growth rate line for an ideal gas subject to Jeans' instability (Sect. 2.3). All curve slopes correspond initially to the predicted Jeans' growth rate. The initial steep growth and the small time delay are caused by the initial noise in the particle distribution. Thus, a certain time is needed for the perturbation to overcome the noise.

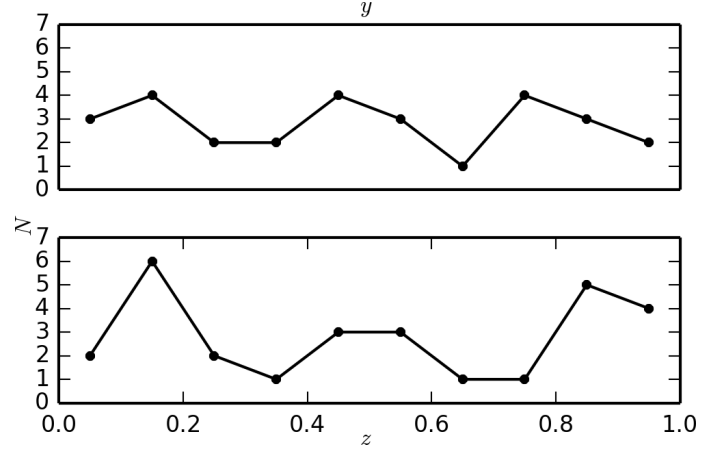


**Fig. 20.** Distribution of y- and z-coordinates of "planetoid" center of mass on a 10x10 grid all OPGs simulations at  $t = 2.5\tau$ .

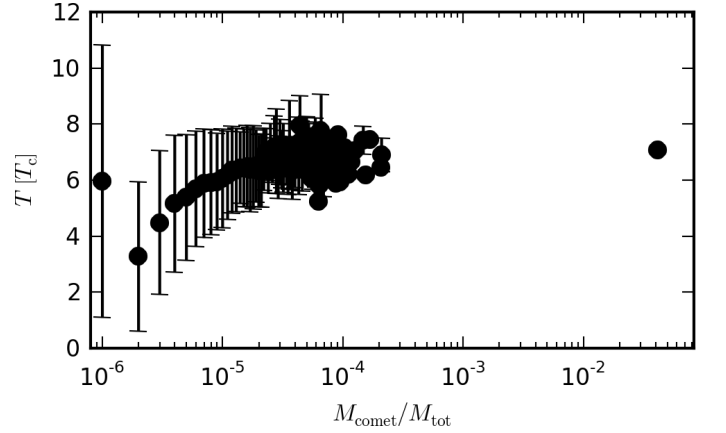


**Fig. 21.** Temperature distribution of unbound molecules and "comets" as a function of "comet" mass of OPGs with  $N_{\text{SM}} = 100^3$  at  $t = 4\tau$ .

#### 4.4.2. "Comet" Mass Distribution

Figure 33 shows snapshots and Fig. 34 the "comet" mass distribution at different times. During the temperature rise, the "comets" are distributed according to a power law:

$$\frac{d \log (\sum M_{\text{comet}})}{d \log (M_{\text{comet}})} = \xi_c \text{ for } M_{\text{comet}} \ll M_{\text{tot}} \quad (43)$$

no "planetoid" is formed. The power law index is very steep at the beginning with  $\xi_c \approx -10$  but quickly decreases for reaching a value of  $\xi_c \approx -2.5$  at the end.

After the temperature increase break at  $t \approx 2.7\tau$ , the power law distribution remains for small "comets", but one bigger "gaseous planetoid" with over 1% of the total mass forms. It is shown in Fig. 19. The spherical body seen at  $t \leq 3\tau$  in the snapshots is uncondensed gas, which is why it does not figure in the "comet" mass distribution (see Sect. 3.4 for a discussion how condensed matter is identified).

A second power law:

$$\frac{d \log (\sum M_{\text{comet}})}{d \log (M_{\text{comet}})} = \xi_p \text{ for } M_{\text{comet}} \gg M_{\text{SM}} \quad (44)$$

on the right side of the diagram describes the "comets" and "planetoids". Each body occurs typically only once with our limited  $N_{\text{SM}}$ , and  $\xi_p = 1$ . Equation (43) describes the mass distribution of small bodies where gravity is negligible whereas Equ.

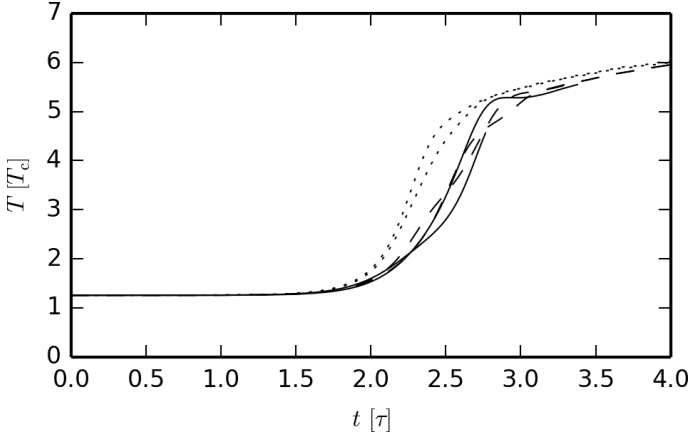


**Fig. 22.** Mean temperature over four one-phase fluid simulations OPGs with different random seeds as a function of time.  $N_{\text{SM}} = 50^3$  and  $64^3$  (dotted line),  $80^3$  and  $100^3$  (dashed line),  $128^3$  and  $160^3$  (solid line).

(44) describes large bodies where gravity is small, but cannot be neglected.

The first high density plane is created thanks to the plane perturbation parallel to the  $yz$ -plane at  $x = 0.5$ . One can observe in Fig. 33 at  $t = 2\tau$  that two filaments form, along to the  $y$ - and  $z$ - axes, connecting the “planetoid” with itself thanks to the periodic boundary conditions. They are aligned with the mesh, but not primarily due to grid effects but because these lines are the shortest distance between the “planetoid” and its periodic images. As can be seen in Fig. 39, diagonal filaments are also possible using the second shortest distance.

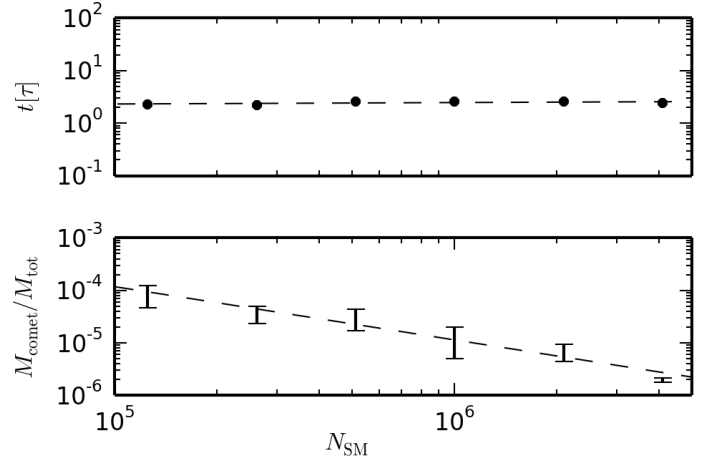
The position of the “planetoid” is, thanks to the plane-wave perturbation, situated in the  $x = 0.5L$  plane, the  $y$  and  $z$  positions are random and depend on the initial condition and vary with every simulation as shown in Fig. 20.

Figure 21 shows the temperature distribution in the “comets” as function of mass. As the number of large “comets” with the same number of super-molecules is small or even one, no error bars can be seen for the larger “comets” and the “gaseous planetoid”.

The broad Maxwellian velocity distribution is seen for the unbound molecules ( $M_{\text{comet}} = 10^{-6}$ ). The small “comets” (2 or more particles) have a clearly smaller temperature and dispersion than the average temperature of the system. This is due to the fact that in order for two super-molecules to cluster together, a third one is needed taking away some of their kinetic energy. The larger a “comet” is, the closer its temperature is to the average one as it has more degrees of freedom. On longer formation time the “planetoids” temperature tends toward the average one as expected.

#### 4.4.3. Scaling

Figure 22 shows the mean temperature value over four simulations with different random seeds. One can see that the two smallest simulations with  $N_{\text{SM}} = 50^3$  and  $64^3$  are starting to collapse earlier than the other simulations, which are very similar. This can be explained by the fact that these simulations have very low  $x_{\text{GLJ}}$  values (Equ. (40)), 3.65 and 4.03  $r_\sigma$ . The first one is in fact lower than the cut-off radius of  $4r_\sigma$  and is in contradiction with Equ. (36), the other one just slightly above it. In these simulations, the gravitational forces are strong even



**Fig. 23.** Time and size of the largest “comet” at the appearance of the turning point.

in short-range inter-molecular interactions, the simulations are therefore over-emphasizing the gravitational effect.

Figure 35 shows the “comet” mass distribution of all OPGs simulations. For small “comets”, the percentage for a same number of super-molecules is the same for all  $N_{\text{SM}}$ . For example, at  $t = 5\tau$ , all simulations have a fraction of  $\sim 10^{-1}$  for comets consisting of two super-molecules. Such small clumps should be called multimers as mentioned below. But, with increasing  $N_{\text{SM}}$ , the mass of a comet consisting of two super-molecules diminishes since  $M_{2\text{SM}} = 2/N_{\text{SM}}$ .

On the other hand, for large “comets” and the “planetoid”, the mass is invariant to  $N_{\text{SM}}$ . For example, the “planetoid” at  $t = 5\tau$  has the same mass of  $M_{\text{planetoid}} \approx 5 \cdot 10^{-2} M_{\text{tot}}$  for all  $N_{\text{SM}}$ .

The fact that the mass distributions are shifted to the left for larger  $N_{\text{SM}}$  is misleading, as shown in Fig. 36. Only the two largest simulations are shown, the simulation with  $N_{\text{SM}} = 128^3$  is shown normally, but for the simulation with  $N_{\text{SM}} = 160^3$  is downscaled to  $160^3/2 \approx 128^3$ , always two “comet” sizes are added together. As can be seen, when comparing the two simulation using the same scaling, the two mass distributions are in fact very similar.

It is interesting to look at the turning point, defined as the point where the mass sum of the biggest “comets” is larger than the mass sum of smaller ones. This point is interesting as it is the first indicator of the creation of a aggregate of molecules that start to be influenced by gravity. Figure 23 shows the time and the mass of the turning point. One can see that the time of appearance is independent of  $N_{\text{SM}}$ . The “comet” mass on the other hand clearly follows a power law with:

$$\frac{M_{\text{comet}}}{M_{\text{tot}}} \approx 10 N_{\text{SM}}^{\xi_N}, \quad (45)$$

with  $\xi_N \approx -1$ . Since  $N_{\text{SM}} = M_{\text{tot}}/M_{\text{SM}}$ , at turning point the number of super-molecules is always of order of 10. In other words, in critical conditions where the attractive molecular force adds up to gravity, the tendency to make a larger condensed body mass fraction starts already with about 10 molecules.

#### 4.4.4. Extrapolation to Physical Scale

Having studied the scaling behavior of the simulations, we can attempt to extrapolate some properties for a fluid consisting of real molecules instead of super-molecules. Considering  $\text{H}_2$

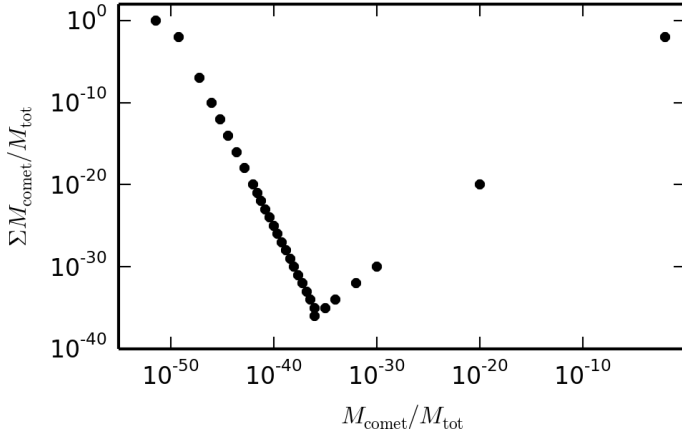


**Fig. 24.** Extrapolation of the “comet” mass-distribution for a real  $\text{H}_2$  molecular fluid at  $t = 5\tau$ .

molecules, the total mass of the OPGs simulations is  $1.4 M_\oplus$ , the box length equal to  $2.3 \cdot 10^{-3}$  AU and  $\tau = 1.5 \cdot 10^{-2}$  years.

Thus, in realistic conditions there would be a total amount of  $2.5 \cdot 10^{51}$   $\text{H}_2$  molecules, the number of molecules per super-molecule  $\eta$  varying from  $2.0 \cdot 10^{46}$  for  $N_{\text{SM}} = 50^3$  to  $3.2 \cdot 10^{44}$  for  $N_{\text{SM}} = 160^3$ . So, even for the largest simulations, there is a difference of number of particles of more than 40 orders of magnitude with real situations. For that reason the extrapolated data has to be treated with caution. As long as no other physics enters in the interval of scales, this is however not extraordinary in regards of common practices in simulation works, such as, e.g., simulating stars with SPH particles. While a single SPH particle can at best represent a mass fraction of  $10^{-6} - 10^{-10}$  of the total, an SPH particle is supposed to behave as the smallest mass element in local thermal equilibrium, say a few 1000 protons over the stellar mass:  $\sim 10^{-55}$ , which lies therefore well over  $10^{40}$  times the SPH simulation resolving capacity.

As can be observed in Fig. 15, the fraction of bound molecules does not change when increasing the number of particles and will remain unchanged for a fluid consisting of molecules. The same is true for the size of the resulting “planetoid”, as can be seen in Fig. 35. Therefore, we can assume that after  $5\tau$ , the system will consist of  $\sim 80\%$  unbound molecules and a “planetoid” with a mass of  $\sim 0.07 M_\oplus$ .

At  $t = 5\tau$ , there is a fraction of  $10^{-1}$  of two molecules aggregates, i.e., dimers, with a mass of  $6.6 \cdot 10^{-27}$  kg. Such multi-molecules clumps should be called “multimers” instead of “comets”. As mentioned above the turning point occurs at  $\sim 2.4\tau$  for always of order of 10 molecules, so its mass is about  $20 m_{\text{H}} = 3.3 \cdot 10^{-26}$  kg.

Using the above values and the two power laws of Equ. (43 – 44), Fig. 24 shows a schematic diagram showing the mass distribution at  $t = 5\tau$ . While the mass fraction of the turning point multimers is tiny, the power law distribution rapidly increases the mass in larger grain- and comet-sized bodies until reaching a planetoid mass.

#### 4.5. Phase Transition

Several physical conditions close to a phase transition are studied. Table 5 summarizes their properties. Three different densities,  $10^{-1}$ ,  $10^{-2}$  and  $10^{-3} n_{\text{cr}}$  and three different temperatures,  $0.1$ ,  $0.2$  and  $0.3 T_{\text{cr}}$  are chosen. As the one-phase fluid studied in Sect. 4.4 also has a density of  $10^{-2} n_{\text{cr}}$ , three additional temperatures,  $0.5$ ,  $0.7$  and  $0.9 T_{\text{cr}}$  were used for this density to make

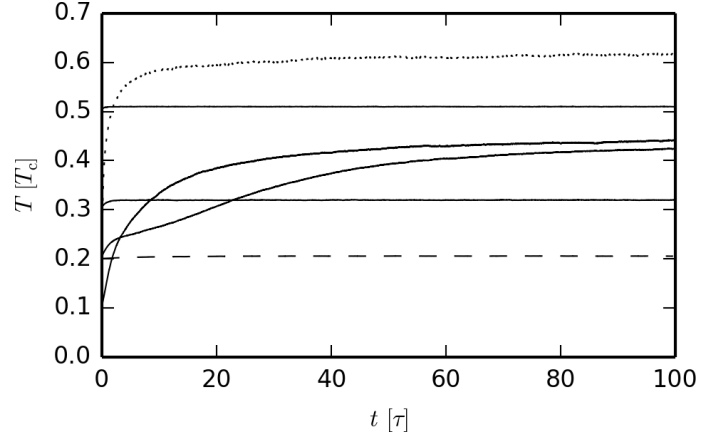


**Fig. 26.** Temperature of non-gravitating fluids as a function of time. Dotted line:  $n = 10^{-1} n_{\text{cr}}$ ; solid line:  $n = 10^{-2} n_{\text{cr}}$ ; dashed line:  $n = 10^{-3} n_{\text{cr}}$ . All simulations with  $N_{\text{SM}} = 50^3$ .

a link between the one-phase fluid and the fluids studied in this section.

Looking at the phase transition diagram (Fig. 25), all fluids with  $T \leq 0.3 T_{\text{cr}}$  are on the Maxwell line. The ones with  $\rho \leq 10^{-2} \rho_{\text{c}}$  are on the  $(\partial P / \partial \rho)_s > 0$  part of the van der Waals phase diagram, which corresponds to meta-stable states on the verge of a deep phase transition. The fluids with  $\rho = 10^{-1} \rho_{\text{c}}$  are on the  $(\partial P / \partial \rho)_s \leq 0$  part of the van der Waals phase diagram, which corresponds to unstable states in a phase transition. The fluids with  $T \geq 0.5 T_{\text{cr}}$  are still in the stable regime.

Three different cases are studied: without gravity, strongly self-gravitating above the Jeans criterion and weakly self-gravitating below the Jeans criterion.

##### 4.5.1. Fluid without gravity

To study the evolution of fluids presenting a phase transition without gravity, the  $x_{\text{GLJ}}$  value has not to be considered and the number of super-molecules is set to  $N_{\text{SM}} = 50^3$ . Figure 26 shows the temperature evolution of some of these fluids. In the beginning, the molecules merge into small “comets”, which leads to a decrease of the potential energy and therefore a rise of the temperature. Once the temperature is high enough, the kinetic and potential energy reach a equilibrium and the fluid remains stable.

The number of “comets” formed is dependent on the density and inversely on the temperature. The higher the number of formed “comets”, the longer it takes for the fluid to reach a stable regime (for example, the the very cold fluids PT1-2 and PT2-2 fluids only reach an asymptotic value around  $t \approx 100\tau$ ).

The “comets” remain at moderate size as can be seen in the snapshots (Fig. 37) and in their mass distribution (Fig. 38): The number of super-molecules per “comets” is  $< 10^{-2} N_{\text{SM}}$ . The mass distribution follows the power law of Equ. (43), but at  $\sim 10^{-4}$ , the mass distribution rises again, presenting a big number of “comets” between  $10^{-4}$  to  $10^{-2}$  super-molecules. Fig. 27 shows a close-up 3D view of a medium sized “comet” and smaller aggregates.

Figure 28 shows the temperature distribution as a function of the “comet” mass. As in simulation OPGs, the temperature for small bodies lies below the average, but reaches the average value for more massive bodies.

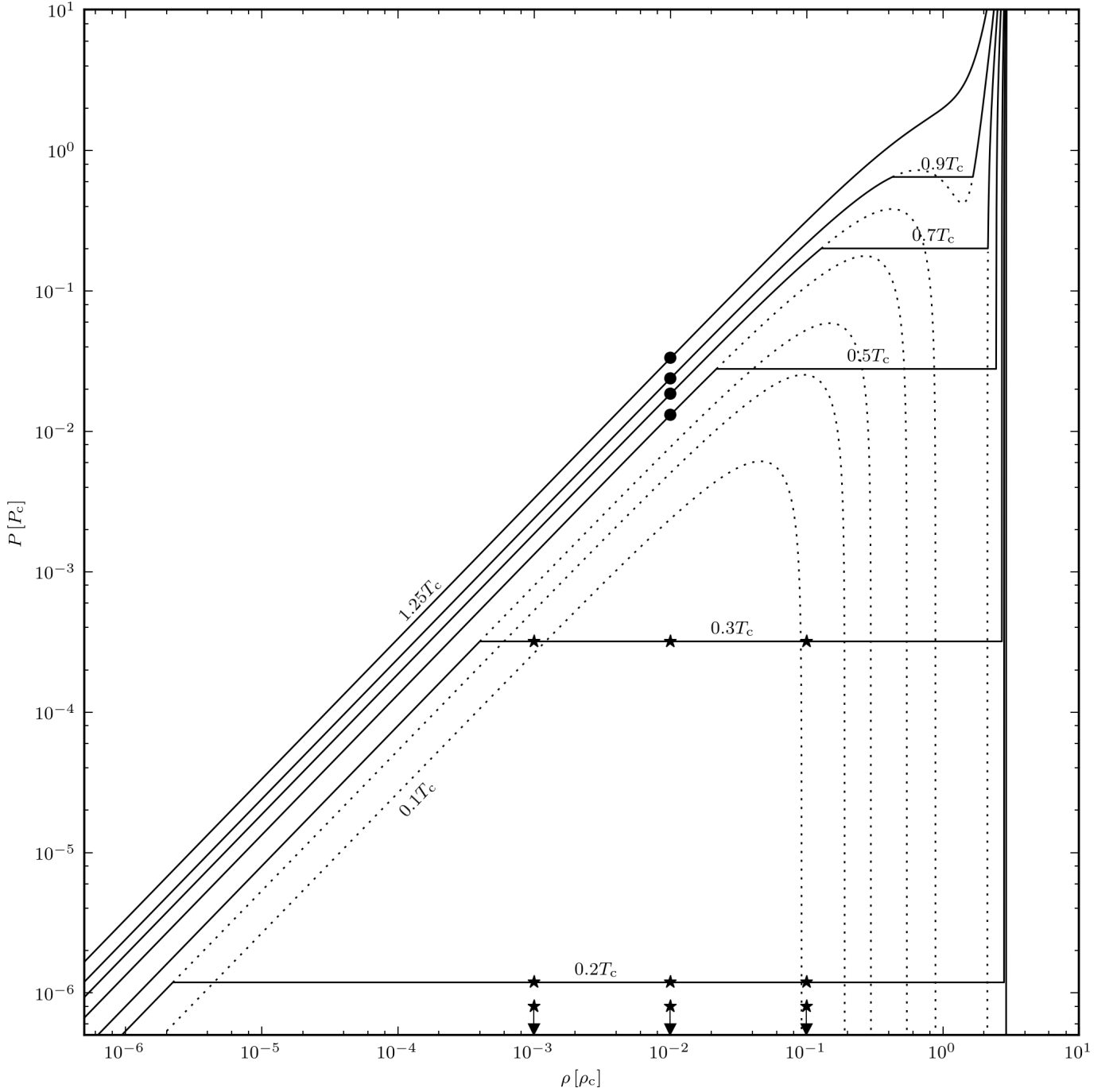


**Fig. 25.** Position of the LJ simulations in a corresponding van der Waals phase diagram. Solid line: Maxwell construct for the van der Waals EOS; dotted line: van der Waals EOS. Star: fluid presenting a phase transition; bullet: one-phase fluid.

#### 4.5.2. Self-gravitating Fluid above Jeans Criterion

All sufficiently self-gravitating simulations use the same gravitational potential,  $G = 1.25 G_J$  ( $T = 1.25 T_{cr}$ ,  $n = 0.01 n_{cr}$ ). As the temperatures and densities differ,  $G_J$  and therefore  $\gamma_J$  is different for each simulations (but always  $> 1$ ).

As  $\gamma_J > 1$  for all simulated fluids, they are unstable if perturbed. The lower the initial temperature of a fluid, the bigger is  $\gamma_J$ , which translates to a faster exponential growth. This can be seen in Fig. 29 where the fluids with a density of  $10^{-2} n_{cr}$  are starting to collapse one after the others, from the lowest temperature to the highest one.

The evolution of the fluids is identical to the fluid OPGs: An exponential rise of the temperature until it reaches a temperature break, after which the temperature rises only slowly and a single “gaseous planetoid” is formed. Figures 39 and 40 show snapshots and “comet” mass distribution, again very similar to the fluid OPGs: First there is a formation of small “comets” following the power law of Equ. (43), then, the “comets” are massive enough to attract each other and merge into one big spherical “planetoid” ( $t > 1\tau$ ) following the power law of Equ. (44). The power law index  $\xi_c$  also evolves in similar fashion as in simulation OPGs, starting very steep and reaching a final value of  $\approx -2$ .

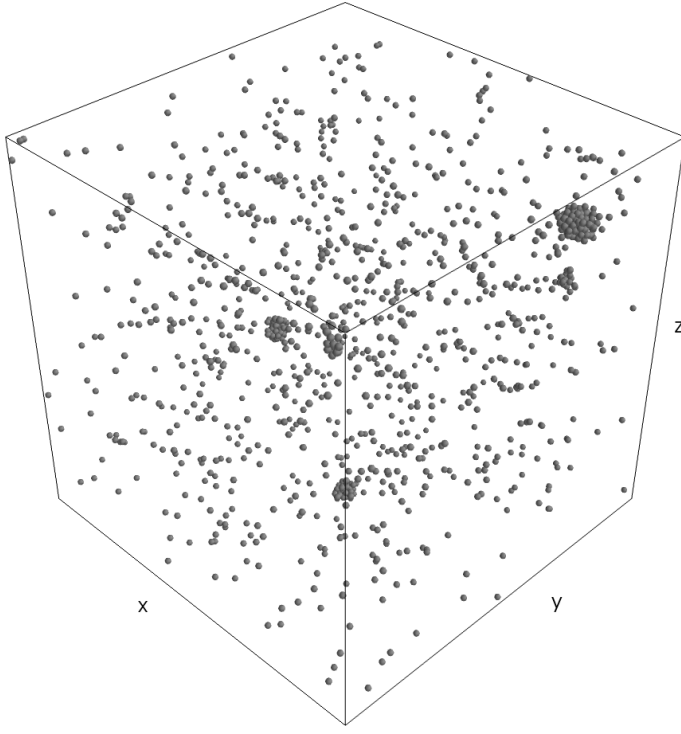


**Fig. 27.** Close-up 3D-view of a medium sized “comet” and smaller aggregates.

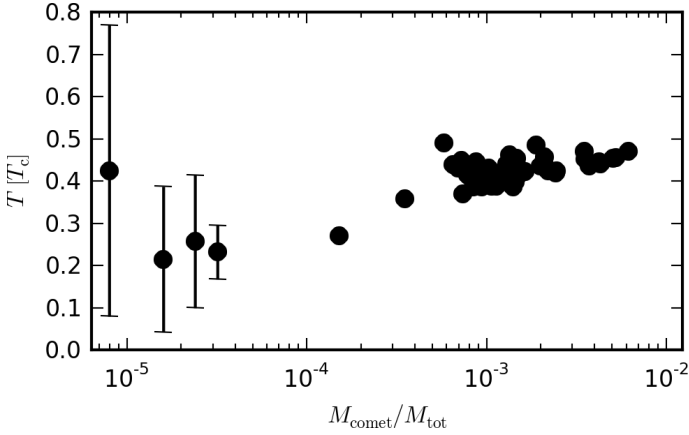


**Fig. 28.** Temperature distribution of unbound molecules and “comets” as a function of “comet” size of PT2-2 without gravity and  $N_{SM} = 50^3$  at  $t = 100\tau$ .

#### 4.5.3. Self-gravitating Fluid below Jeans Criterion

In order to compare weakly self-gravitating fluids in a phase transition (on the Maxwell line) with out-of-phase-transition ones (below the Maxwell line),  $\gamma_I$  is set to 0.5 for all fluids. This means that the individual  $G$  value is different for each simulation.

As shown in Sect. 4.5.1, the perturbation of the weakly self-gravitating one-phase fluid OPGw does not create any effect if  $\gamma_I < 1$ . Figure 30 shows the temperature as a function of time of the self-gravitating fluids PT5-2, PT3-2 and PT2-2, and compares them to the non-gravitating fluids. The out-of-phase-transition fluid PT5-2 remains unchanged and does not differ from the non-gravitating fluid, identical to OPGw.

The temperatures of the fluids in a phase transition PT3-2 and PT2-2 are exponentially growing and differ clearly from the

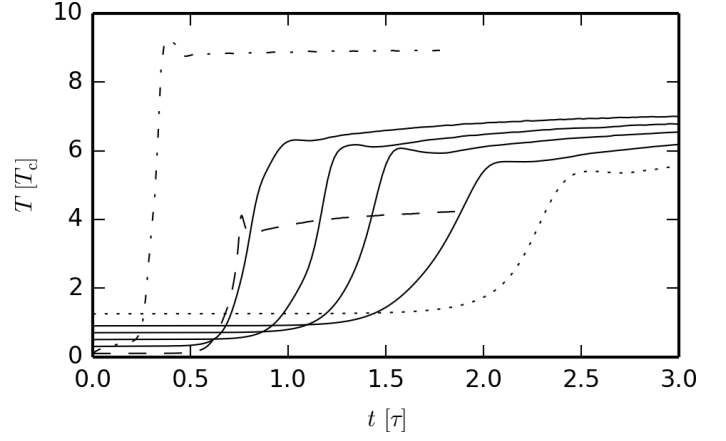


**Fig. 29.** Temperature of sufficiently self-gravitating fluids as a function of time. Dotted line: OPGs; dashed line: PT1-3; solid line (from left to right): PT3-2, PT5-2, PT7-2, PT9-2; dash-dotted line: PT1-1. All simulations with  $N_{SM} = 100^3$ .

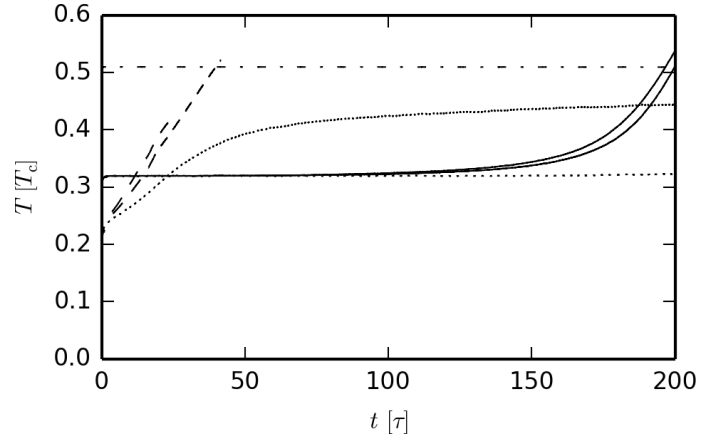


**Fig. 30.** Temperature of weakly self-gravitating fluids as a function of time. Dotted line: PT2-2 and PT3-2 with  $N_{SM} = 50^3$  and without gravity; dashed line: PT2-2,  $\gamma_I = 0.5$  and  $N_{SM} = 80^3$  and  $100^3$ ; solid line PT3-2  $\gamma_I = 0.5$  and  $N_{SM} = 80^3$  and  $100^3$ ; dash-dotted line PT5-2,  $\gamma_I = 0.5$  and  $N_{SM} = 100^3$ .

non-gravitating ones. In the beginning, the LJ forces are dominating the gravitational ones and the fluids are behaving like non-gravitating fluids. PT2-2 is reacting much faster than PT3-2, thanks to its low initial temperature and the fluctuations due to the Maxwellian velocity distribution, forms many small and medium-sized “comets” (see Sect. 4.5.1). Once these “comets” are formed, their mass is high enough to attract each other by gravity, forming a single “rocky planetoid”.

This can be seen in the snapshots (Fig. 41) and “comet” mass distribution (Fig. 42). During the first  $15\tau$ , the fluid is identical to the low-temperature non-gravitating fluid (compare to Fig. 38). Only then does gravity start to play a role, one can see the formation of a “planetoid” and how the small and medium-sized “comets” are swallowed by it during its growth.

Having a higher temperature, PT3-2 does form almost no small or medium-sized “comets” which can be seen in the snapshots (Fig. 43) and “comet” mass distribution (Fig. 44) for the first  $\approx 50\tau$ . Only after  $50\tau$  does gravity show its effect by the appearance of a medium-sized “comet”, being too massive to fit into the power law  $\xi_1$  (see Fig. 43,  $t = 50\tau$ ). From then on, this

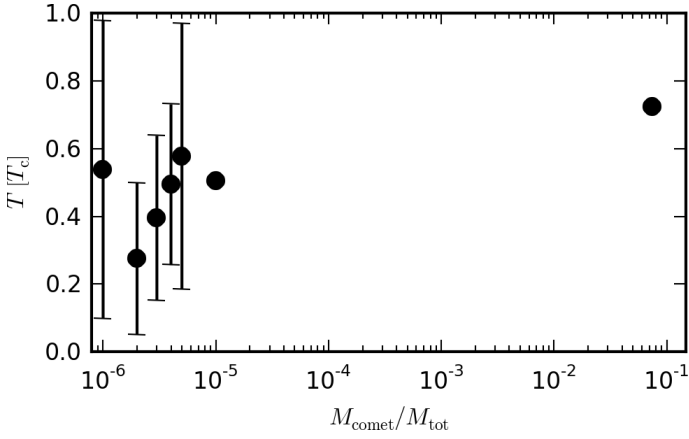


**Fig. 31.** Temperature distribution of unbound molecules and “comets” as a function of “comet” size of PT3-2 with  $\gamma_J = 0.5$  and  $N_{SM} = 100^3$  at  $t = 200\tau$ .

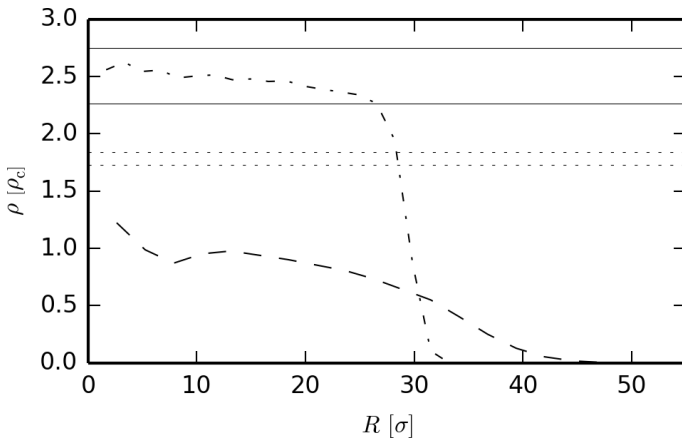


**Fig. 32.** Density of “planetoid” as a function of the radius. Dashed line: OPGs with  $N_{SM} = 100^3$  at  $t = 4\tau$ , the “gaseous planetoid” consists of 41559 super-molecules ( $0.042 M_{tot}$ ). Dash-Dotted line: PT3-2 with  $\gamma_J = 0.5$  and  $N_{SM} = 100^3$  at  $t = 200\tau$ , the “rocky planetoid” consists of 74208 super-molecules ( $0.074 M_{tot}$ ). Solid lines: hydrogen, higher value: solid; lower value: liquid. Dotted line:  $\rho_f$  of Lagrange-Jacobi identity, higher value: SC; lower value: HCP/FCC.

“comet” is attracting super-molecules and thus growing in size until at  $t \approx 125\tau$ , a single big “rocky planetoid” is formed.

Figure 31 shows the temperature distribution as a function of the “comet” mass of PT3-2. The temperature of the “comets” containing few super-molecules lies below the average, but the “planetoids” temperature is the same as the average.

PT2-2, PT3-2 and PT5-2 are all scaling very well. The two fluids in a phase transition, PT2-2 and PT3-2, have a almost identical timescale for the exponential growth for  $N_{SM} = 80^3$  and  $100^3$ , the slight difference is due to the initial random seed. As  $\chi_{GLJ}$  depends on  $\gamma_J$  and the temperature, both much lower than for OPGs, its value is clearly above the cut-off radius, 7.63 and 8.34 for PT2-2 and 7.03 and 7.69 for PT3-2.

PT5-2 shows no difference for any number of super-molecules, with  $N_{SM}$  ranging from  $50^3$  to  $100^3$ .

#### 4.6. “Planetoid” densities

Figure 32 shows the densities of the “planetoids” as a function the radius of the simulations OPGs and PT3-2 with  $\gamma = 0.5\gamma_J$ , and compares them to hydrogen laboratory data and the values found in the Lagrange-Jacobi identity (Sect. 2.2).

The density of the OPGs “gaseous planetoid” is below the one of a conventional solid or liquid. As their temperature is above the critical value ( $T > 6 T_{cr}$ ), the super-molecules are not able to condense without the aid of gravity and, due to their high kinetic energy, are vibrating at much higher amplitudes, leading to more space between the super-molecules and therefore a lower density compared to super-molecules below the critical temperature.

The density of the “gaseous planetoid” is dropping with increasing radius, it does hence not qualify as a homogeneous sphere, but its average density is below the  $\rho_f$  value of the Lagrange-Jacobi identity (Equ. (13)), in accordance with Tab. 2 and Fig. 8 for “gaseous planetoids”.

The density of the PT3-2 “rocky planetoid” lies between the liquid and the solid phase. There is no continuous density drop as for the OPGs simulation, the density remains stable up to almost the outer radius and the body can be approximated as a homogeneous sphere. Its density lies above  $\rho_f$  in accordance with Tab. 2 and Fig. 8 for “rocky planetoids”.

## 5. Conclusions

Analytic methods (Sect. 2) and computer simulations (Sects. 3-4) have been used to study sub-stellar fragmentation of fluids presenting a phase transition. The motivating astrophysical context are molecular clouds where  $H_2$  forms the bulk of the gravitating mass and is not very far from condensation conditions.

### 5.1. Analytic Results

The study of the Virial theorem using the gravitational and the Lennard-Jones potential energies has shown that there is a maximum temperature below which a fluid can fragment at arbitrary low masses. It is interesting that this temperature is an order of magnitude above the critical temperature. This shows, granted the right circumstances, that “comets” can form at temperatures an order of magnitude larger than the critical temperature. In the case of  $H_2$ , this maximum temperature lies in the range of 400 – 600 K depending on the solid crystalline structure.

A van der Waals fluid can be in three different states: gaseous, solid/liquid, or in a phase transition where the two phases coexist. The latter is defined by lying on the line of the Maxwell construct, where  $(\partial P / \partial \rho)_s = 0$ . A fluid is gravitationally unstable if an introduced perturbation has a wavelength above a certain value, which depends on  $(\partial P / \partial \rho)_s$ . Since this quantity vanishes for a fluid presenting a phase transition, such a fluid is also gravitationally unstable.

### 5.2. Simulation Results

Simulations have been performed using the state of the art molecular dynamics simulator LAMMPS. Super-molecules have been used in order to simulate the gravitational and the molecular forces together with a computationally tractable number of particles.



### 5.2.1. Super-Molecules

The super-molecule concept has been tested thoroughly. Good scaling is achieved for non-gravitational effects if the number of super-molecules is large enough ( $\gtrsim 10^5$ ). The sticking point for gravitational effects is to assure that the molecular LJ forces are dominating the gravitational ones in close-range interactions. This is achieved by setting the number of super-molecules large enough so that the distance at which the two forces are equal is above the cut-off radius, i.e.  $\geq 4\sigma_{\text{SM}}$ . For a  $\text{H}_2$  fluid this sets a maximum super-molecule mass equal to  $5.7 \cdot 10^{-6} M_{\oplus}$ , limiting the total mass that can be simulated by the available computing power.

In principle the super-molecule concept should not perfectly reproduce the time-dependence of diffusive properties, as bigger particles introduce faster relaxation. But our experiments using several orders of magnitude different resolutions did not reveal important modifications in the timings of major collapse and asymptotic evolution state. This enables us to study the fragmentation of large bodies which we call “comets” and “planetoids”.

### 5.2.2. One-Phase Fluid

A plane sinusoidal perturbation has been applied into a one-phase fluid with a temperature above the critical value. The results reproduce the ideal gas Jeans instability: no collapse is seen for conditions below the Jeans criterion while an exponential growth of the perturbation is observed for conditions above it.

As a result, the temperature rises, and small and medium-sized “comets” form, some of which later merge into one big “planetoid”. An interesting observation is the mass distribution of these “comets”, which follows a power law for the small and medium-sized ones, while the “planetoid” and the largest “comets” follow a different power law.

### 5.2.3. Phase Transition Fluid

Fluids with a temperature below the critical value and close to the effective phase transition have been simulated for three different cases: without gravity, sufficiently and weakly self-gravitating (above and below the ideal gas Jeans criterion).

Due to the Maxwellian velocity distribution fluctuations, the non-gravitating fluids form small and medium-sized “comets” until the potential and kinetic energy reach an equilibrium; thereafter they remain statistically stable. In the absence of any long-range force, no “planetoid” forms.

The self-gravitating fluids with a gravitational potential above the ideal-gas Jeans criterion do not react differently to a plane sinusoidal perturbation than a one-phase fluid: the perturbation grows exponentially, its temperature rises and small and medium-sized “comets” form which ultimately merge into one “planetoid”.

The analysis predicts that fluids presenting a phase transition are unstable even if the gravitational potential alone is below the ideal gas Jeans threshold. The performed simulations of weakly self-gravitating fluids in the phase transition regime did reproduce the prediction. Due to the weak nature of the gravitational potential, the time-scale to see this reactions is two orders of magnitude longer than for sufficiently self-gravitating fluids, but in the end, a big central “planetoid” forms anyway. While the out-of-phase-transition fluids do not amplify perturbations, those in a phase transition indeed amplify them.

This study is general enough to be relevant for many astrophysical situations. In the case of  $\text{H}_2$  as main component, it concerns situations where temperature may drop well below 10 K, such as in cold molecular gas in the outer galactic disks, in expanding winds of planetary nebulae or supernovae where cold sub-stellar mass condensations are known to form, or in protoplanetary disks. Other molecules besides  $\text{H}_2$ , such as CO, can condense even sooner, but as their mass fraction is small they should not perturb significantly the gravitational balance, while He should not condense at all and keep a minimal amount of gaseous phase.<sup>2</sup> The precipitation of formed “comets” and “planetoids” in a gravitational field, separating the gaseous and condensed phases, is also a fascinating aspect that is as yet impossible to capture with traditional hydrodynamical codes but possible with the molecular dynamics approach.

Further simulation work including more specific astrophysical applications are pursued.

*Acknowledgements.* This work is supported by the STARFORM Sinergia Project funded by the Swiss National Science Foundation.

We thank the LAMMPS team for providing a powerful open source tool to the scientific community.

We thank the referee for a thorough reading of the manuscript and constructive comments which substantially improved the paper.

## References

- Air Liquide. 1976, Gas Encyclopedia (Editor Elsevier)
- Allamandola, L. J., Bernstein, M. P., Sandford, S. A., & Walker, R. L. 1999, *Space Science Reviews*, 90, 219
- Binney, J. & Tremaine, S. 2008, *Galactic Dynamics: Second Edition*
- Bolatto, A. D., Wolfire, M., & Leroy, A. K. 2013, *Annual Review of Astronomy and Astrophysics*, 51, 207
- Buch, V. & Devlin, J. P. 1994, *The Astrophysical Journal Letters*, 431, L135
- Burkert, A. & O’dell, C. R. 1998, *The Astrophysical Journal*, 503, 792
- Carey, V. P. 1999, *Statistical Thermodynamics and Microscale Thermophysics* (Cambridge University Press)
- Clausius, R. 1870, *Annalen der Physik*, 217, 124
- Clerk-Maxwell, J. 1875, *Nature*, 11, 357
- Combes, F. & Pfenniger, D. 1997, *Astronomy and Astrophysics*, 327, 453
- Dissly, R. W., Allen, M., & Anicich, V. G. 1994, *The Astrophysical Journal*, 435, 685
- Draine, B. T. 2011, *Physics of the Interstellar and Intergalactic Medium*
- Elmegreen, B. G. & Scalo, J. 2004, *Annual Review of Astronomy and Astrophysics*, 42, 211
- Ewald, P. P. 1921, *Annalen der Physik*, 369, 253
- Grenier, I. A., Casandjian, J.-M., & Terrier, R. 2005, *Science*, 307, 1292
- Hockney, R. W. & Eastwood, J. W. 1981, *Computer Simulation Using Particles*
- Jeans, J. H. 1902, *Royal Society of London Philosophical Transactions Series A*, 199, 1
- Johnston, D. C. 2014, *ArXiv e-prints*, 1402, 1205
- Jones, J. E. 1924, *Royal Society of London Proceedings Series A*, 106, 463
- Kondepudi, D. K. & Prigogine, I. 1998, *Modern thermodynamics: from heat engines to dissipative structures* (John Wiley)
- Kristensen, L. E., Amiaud, L., Fillion, J.-H., Dulieu, F., & Lemaire, J.-L. 2011, *Astronomy & Astrophysics*, 527, A44
- Langer, W. D., Velusamy, T., Pineda, J. L., et al. 2010, *Astronomy and Astrophysics*, 521, L17
- Lekner, J. 1982, *American Journal of Physics*, 50, 161
- Paradis, D., Dobashi, K., Shimoikura, T., et al. 2012, *Astronomy and Astrophysics*, 543, 103
- Pfenniger, D. 2004, in *IAU Symposium*, Vol. 220, *Dark Matter in Galaxies*, ed. S. Ryder, D. Pisano, M. Walker, & K. Freeman, 241
- Pfenniger, D. & Combes, F. 1994, *Astronomy and Astrophysics*, 285, 94
- Pfenniger, D., Combes, F., & Martinet, L. 1994, *Astronomy and Astrophysics*, 285, 79
- Planck Collaboration, Ade, P. A. R., Aghanim, N., et al. 2011, *Astronomy and Astrophysics*, 536, 19

<sup>2</sup> In Safa & Pfenniger (2008) it was calculated that the mixture of He and  $\text{H}_2$  at cosmic abundance does not change the conclusion regarding the phase transition of  $\text{H}_2$  alone as the species do not remain mixed when  $\text{H}_2$  alone would condensate.

- Plimpton, S. 1995, *Journal of Computational Physics*, 117, 1
- Safa, Y. & Pfenniger, D. 2008, *European Physical Journal B*, 66, 337
- Sahai, R. & Nyman, L.-A. 1997, *The Astrophysical Journal Letters*, 487, L155
- Sandford, S. A. & Allamandola, L. J. 1993, *The Astrophysical Journal Letters*, 409, L65
- Tuckerman, M., Berne, B. J., & Martyna, G. J. 1992, *Journal of Chemical Physics*, 97, 1990
- van der Waals, J. D. 1910, *Koninklijke Nederlandse Akademie van Wetenschappen Proceedings Series B Physical Sciences*, 13, 1253
- Walker, M. A. 2013, *Monthly Notices of the Royal Astronomical Society*, 434, 2814
- Walsh, J. R. & Meaburn, J. 1993, *The Messenger*, 73, 35
- Weinberg, S. 1972, *Gravitation and Cosmology: Principles and Applications of the General Theory of Relativity*

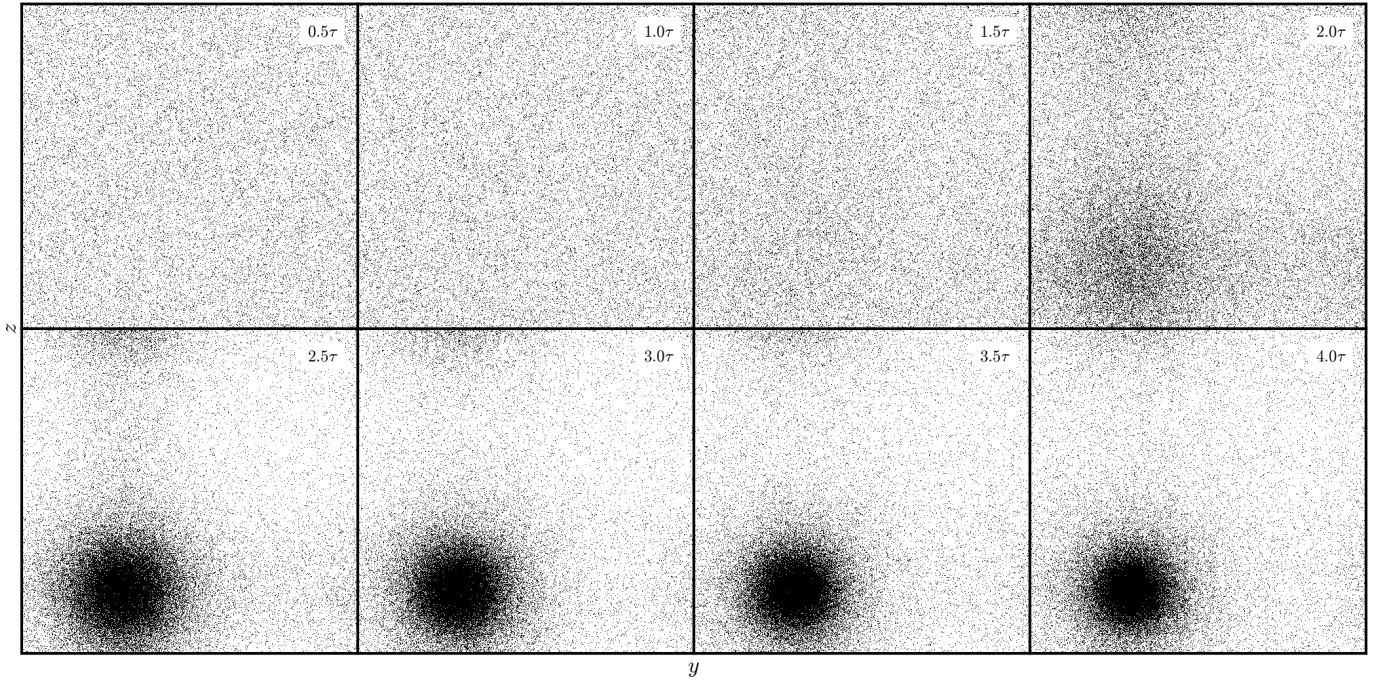


**Fig. 33.** Snapshot time-sequence of the simulation OPGs with  $N_{\text{SM}} = 100^3$  showing the smooth formation of a “planetoid”. The slice size is  $0.025 \times 1 \times 1 L^3$  at  $x = (0.5 \pm 0.0125)L$ .

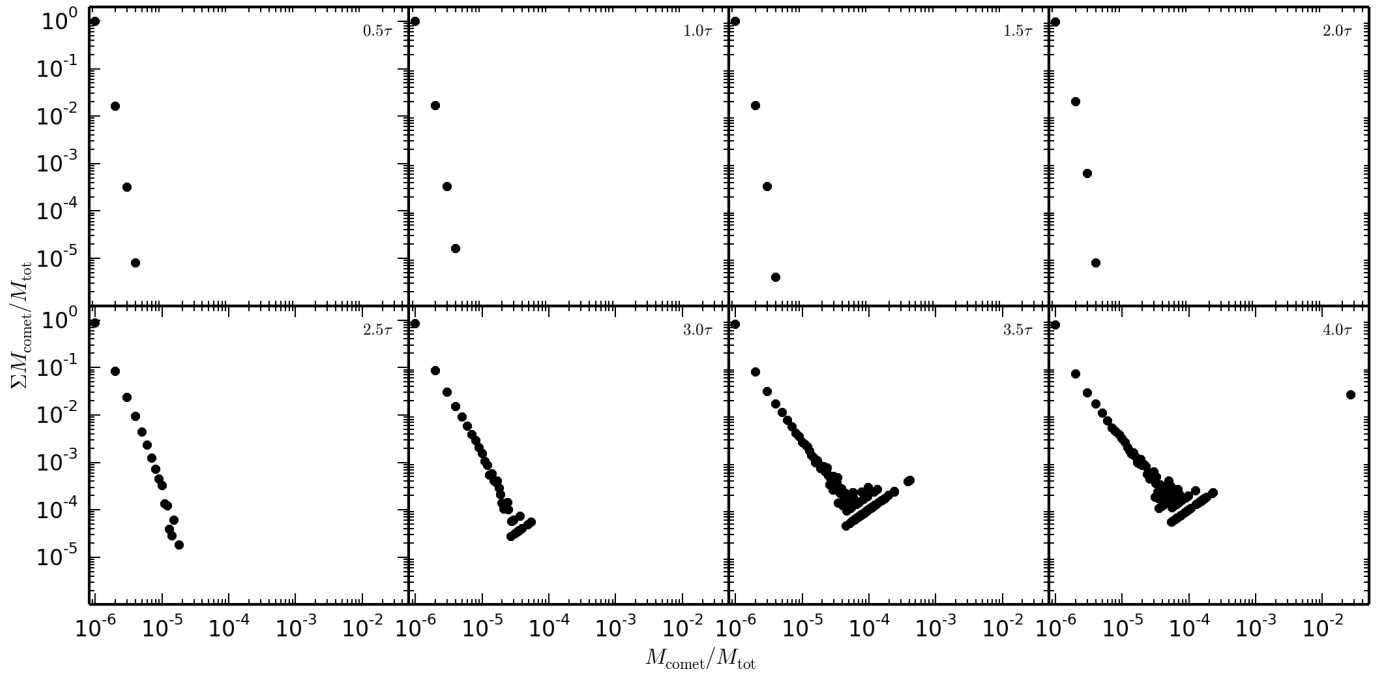


**Fig. 34.** Snapshot “comet” mass-distribution sequence of the simulation OPGs with  $N_{\text{SM}} = 100^3$ .

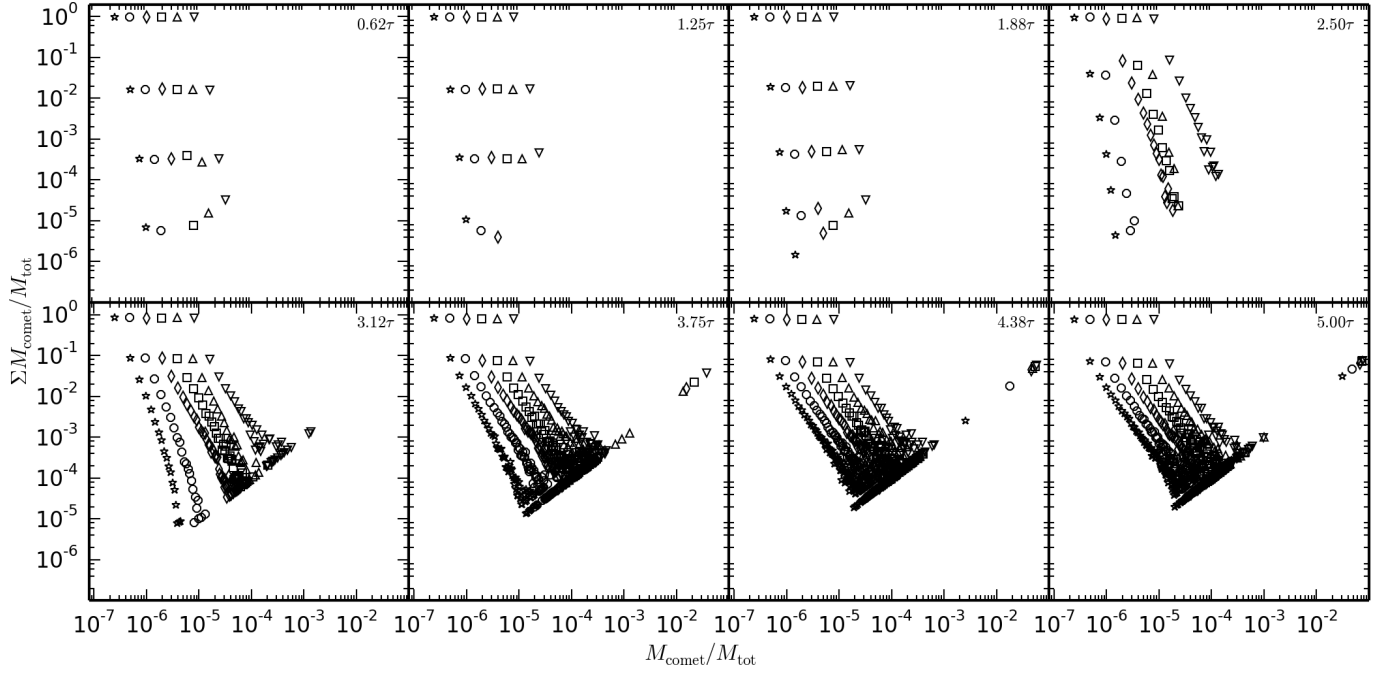


**Fig. 35.** Snapshot “comet” mass-distribution sequence of all OPGs simulations with  $N_{\text{SM}}$  equal to down triangle:  $50^3$ , up triangle:  $64^3$ , square:  $80^3$ , diamond:  $100^3$ , circle:  $128^3$ , star:  $160^3$ .

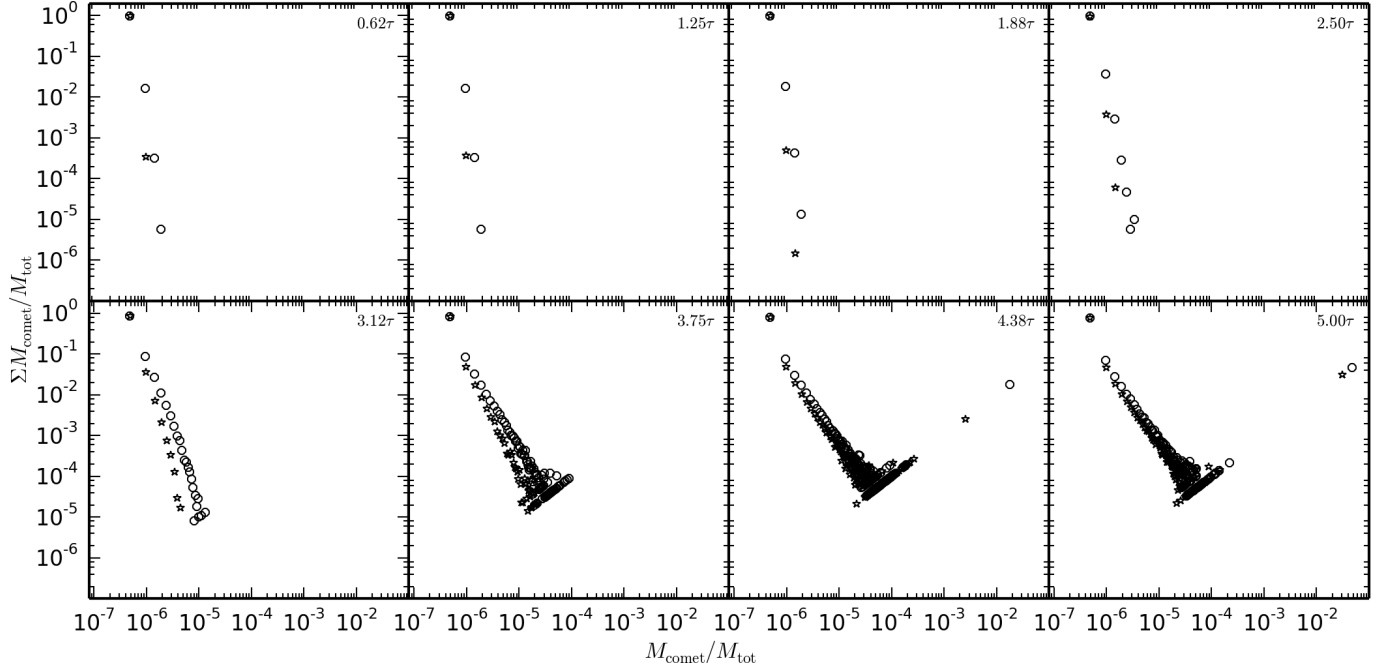


**Fig. 36.** Snapshot “comet” mass-distribution summation sequence of OPGs simulations. Reference with  $N_{\text{SM}} = 128^3$ : circle; sum of 4 “comet”-sizes per star:  $100^3$ .

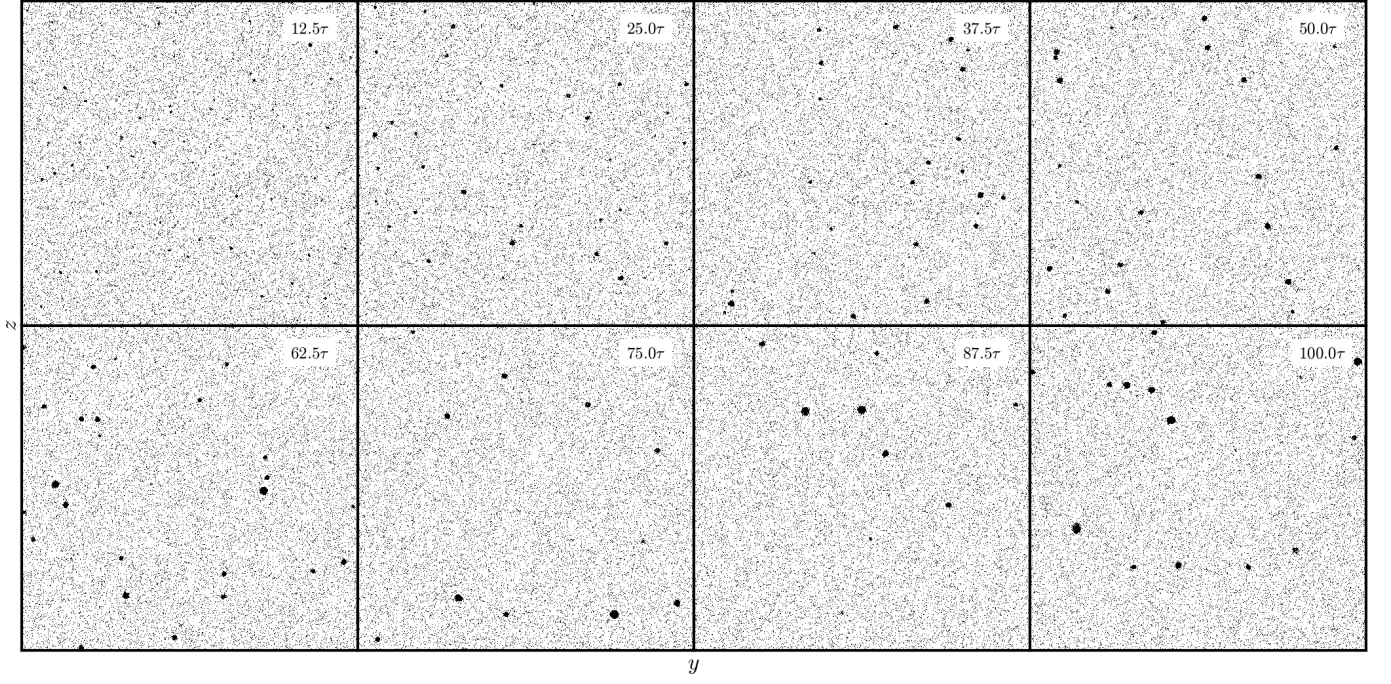


**Fig. 37.**  $0.2 \times 1 \times 1 L^3$  snapshots at  $x = (0.5 \pm 0.1)L$  of simulation PT2-2 with  $N_{\text{SM}} = 50^3$  and without gravity.

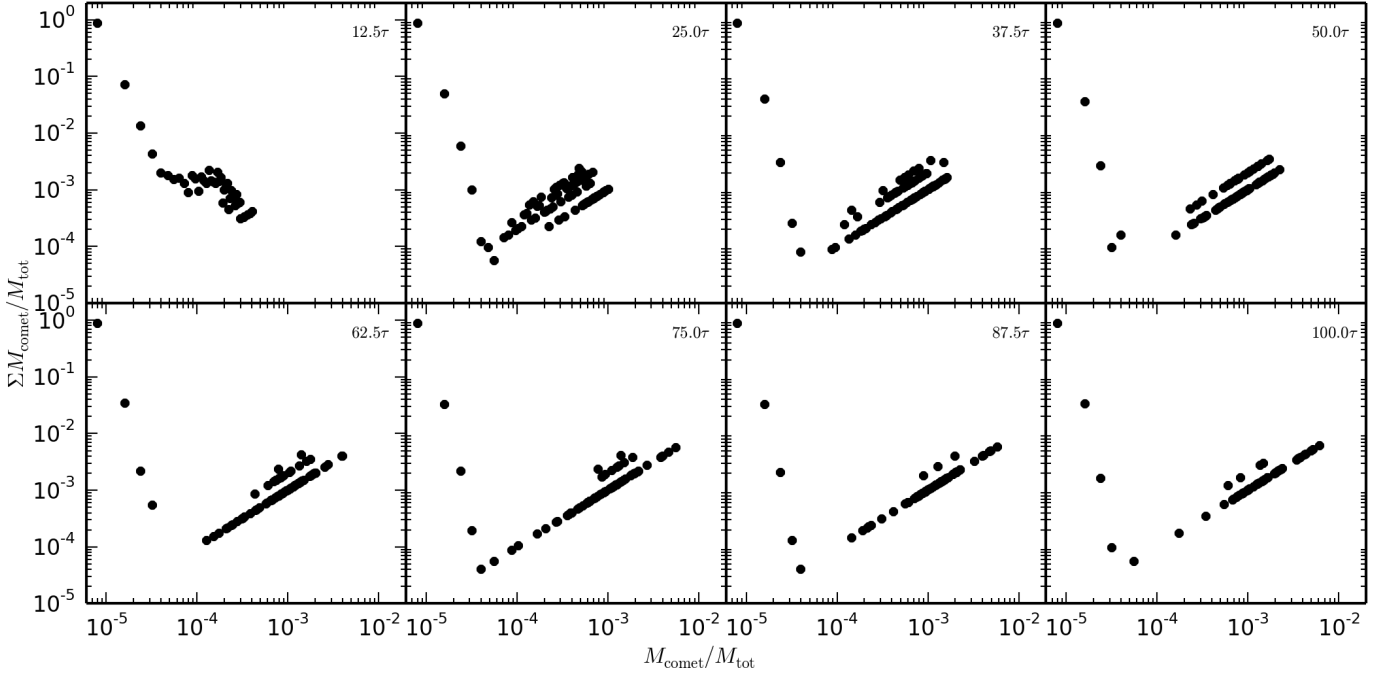


**Fig. 38.** “Comet” mass distribution snapshots of simulation PT2-2 with  $N_{\text{SM}} = 50^3$  and without gravity.

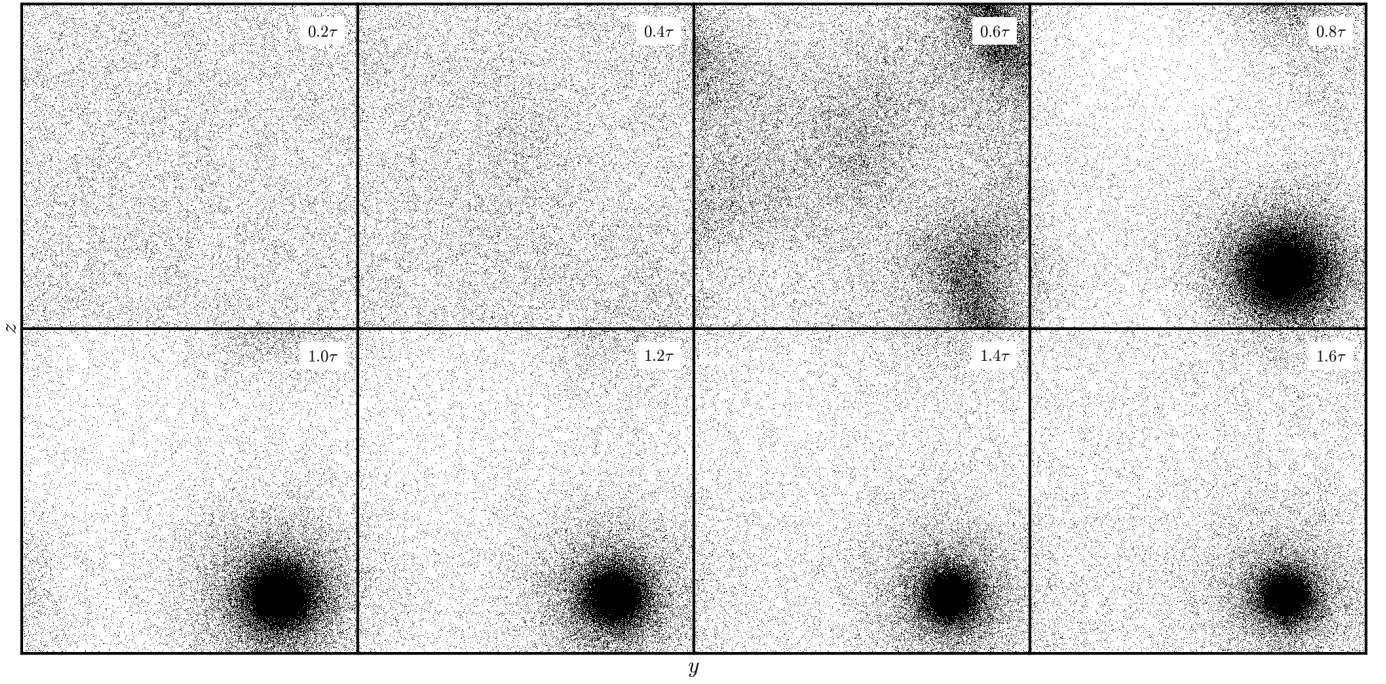


**Fig. 39.**  $0.025 \times 1 \times 1 L^3$  snapshots at  $x = (0.5 \pm 0.0125)L$  of sufficiently self-gravitating simulation PT1-3 with  $N_{\text{SM}} = 100^3$ .

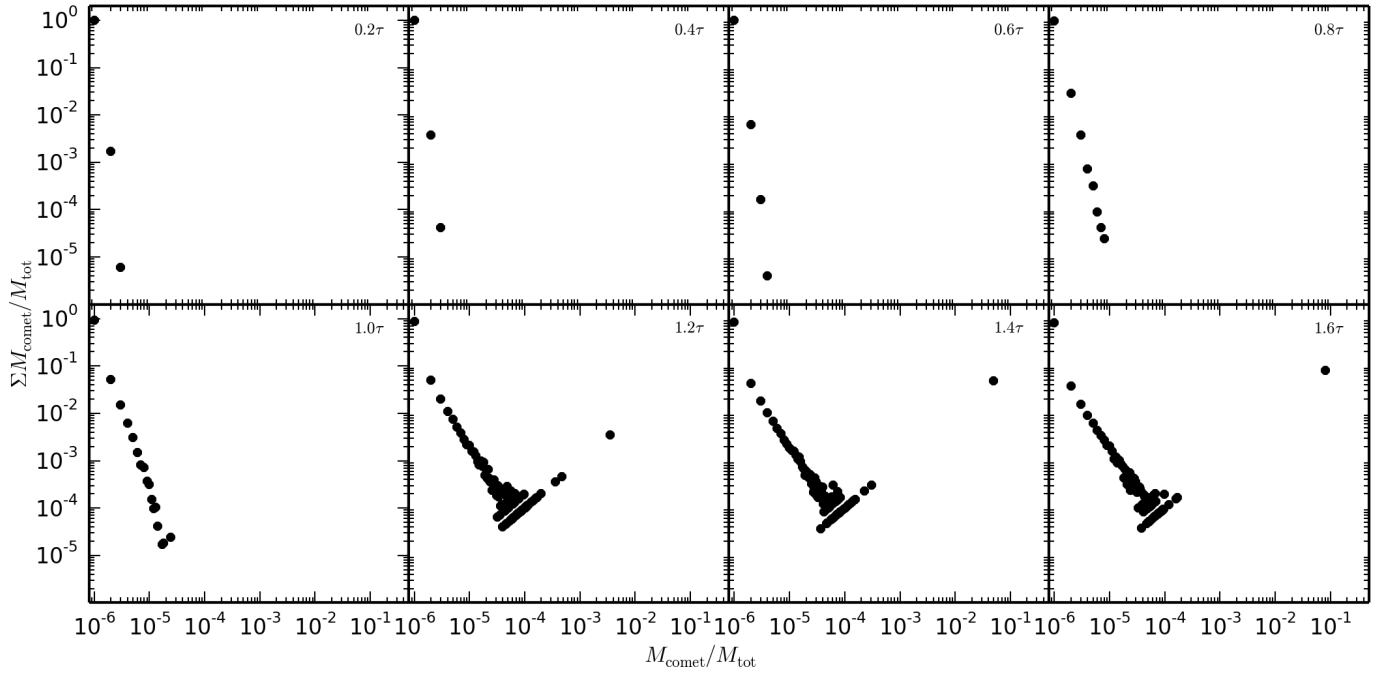


**Fig. 40.** “Comet” mass distribution snapshots of sufficiently self-gravitating simulation PT1-3 with  $N_{\text{SM}} = 100^3$ .

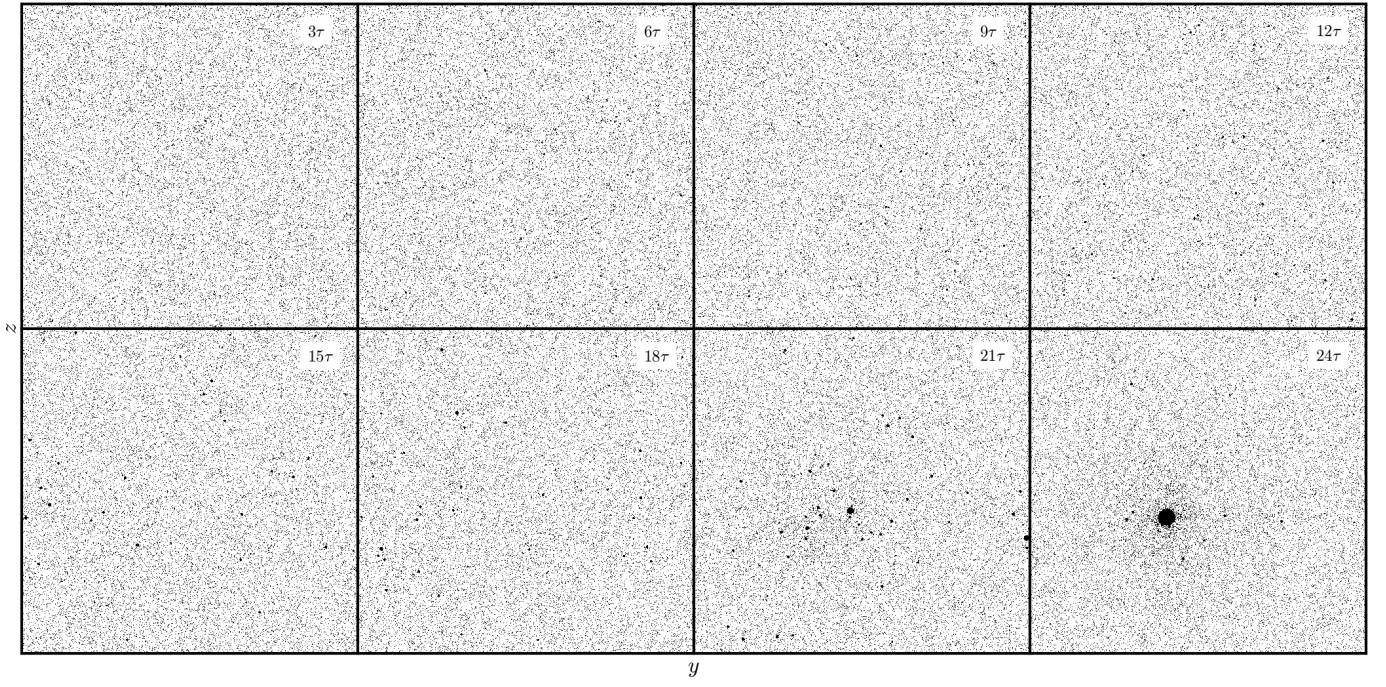


**Fig. 41.**  $0.025 \times 1 \times 1 L^3$  snapshots at  $x = (0.5 \pm 0.0125)L$  of weakly self-gravitating simulation PT2-2 with  $N_{\text{SM}} = 100^3$ .

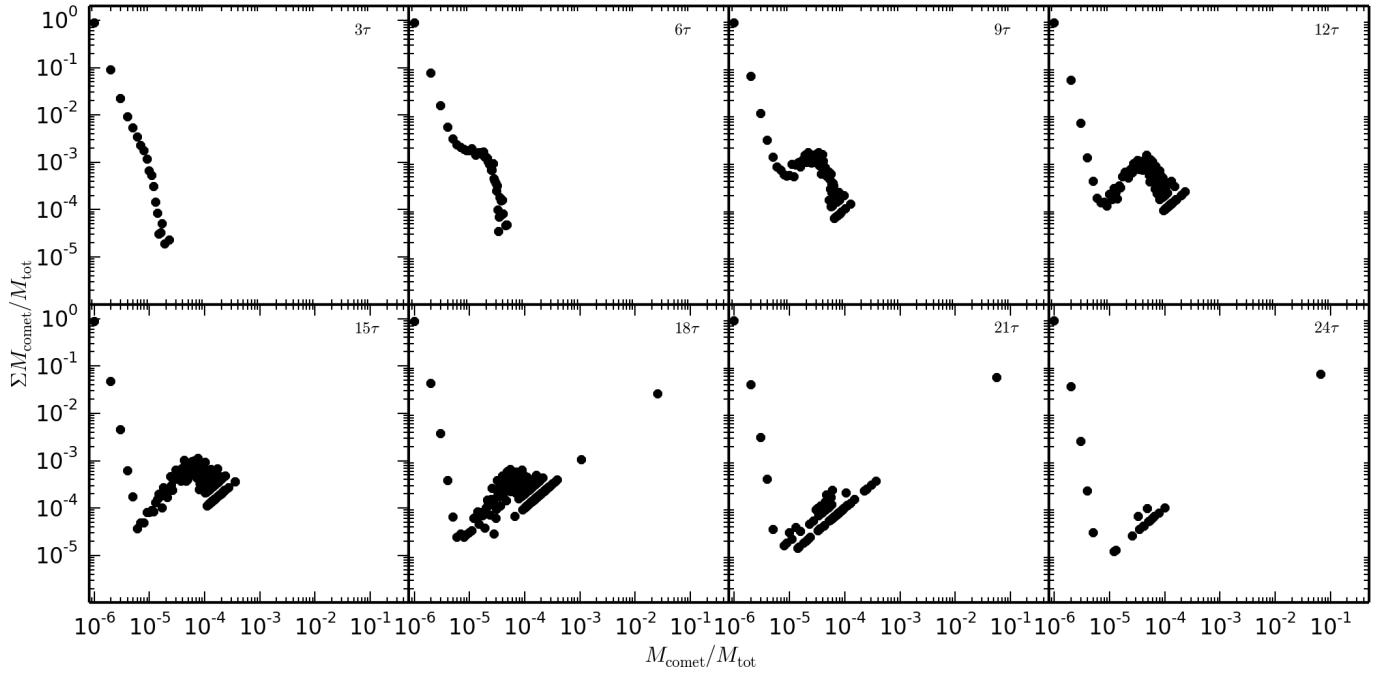


**Fig. 42.** “Comet” mass distribution of weakly self-gravitating simulation PT2-2 with  $N_{\text{SM}} = 100^3$ .

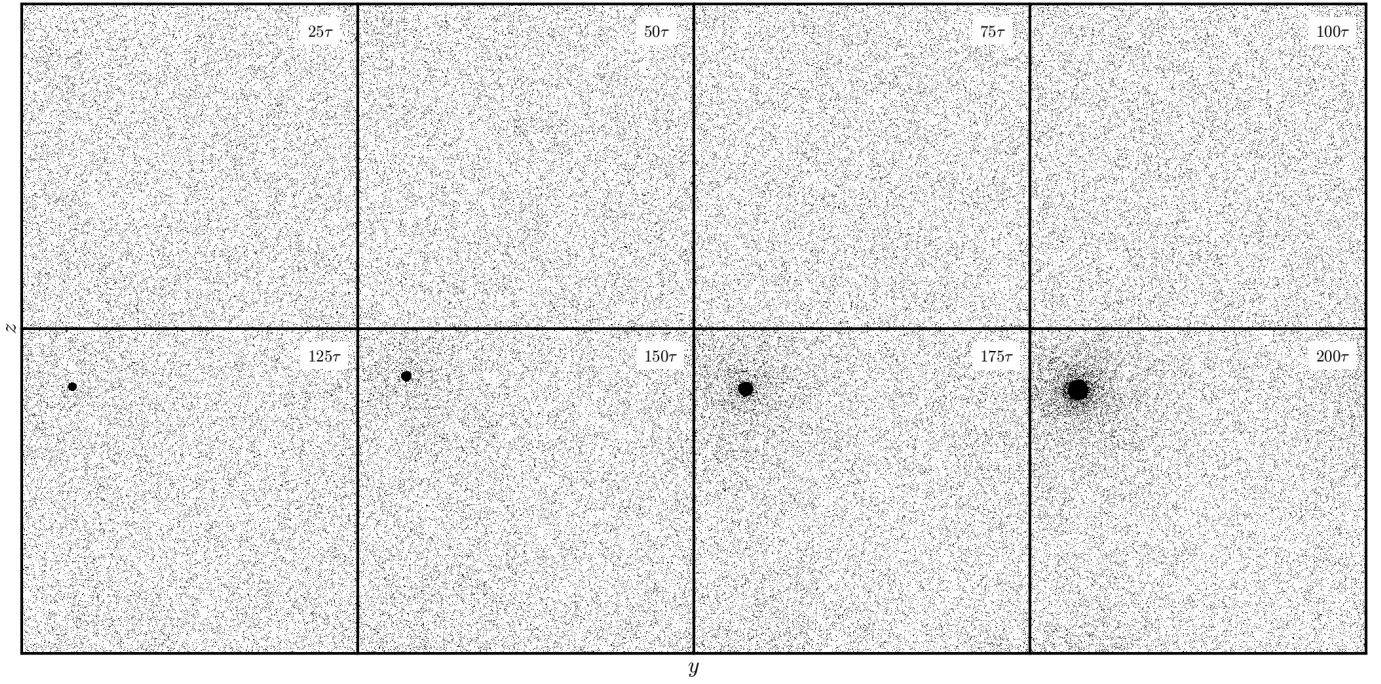


**Fig. 43.**  $0.025 \times 1 \times 1 L^3$  snapshots at  $x = (0.5 \pm 0.0125)L$  of weakly self-gravitating simulation PT3-2 with  $N_{\text{SM}} = 100^3$ .

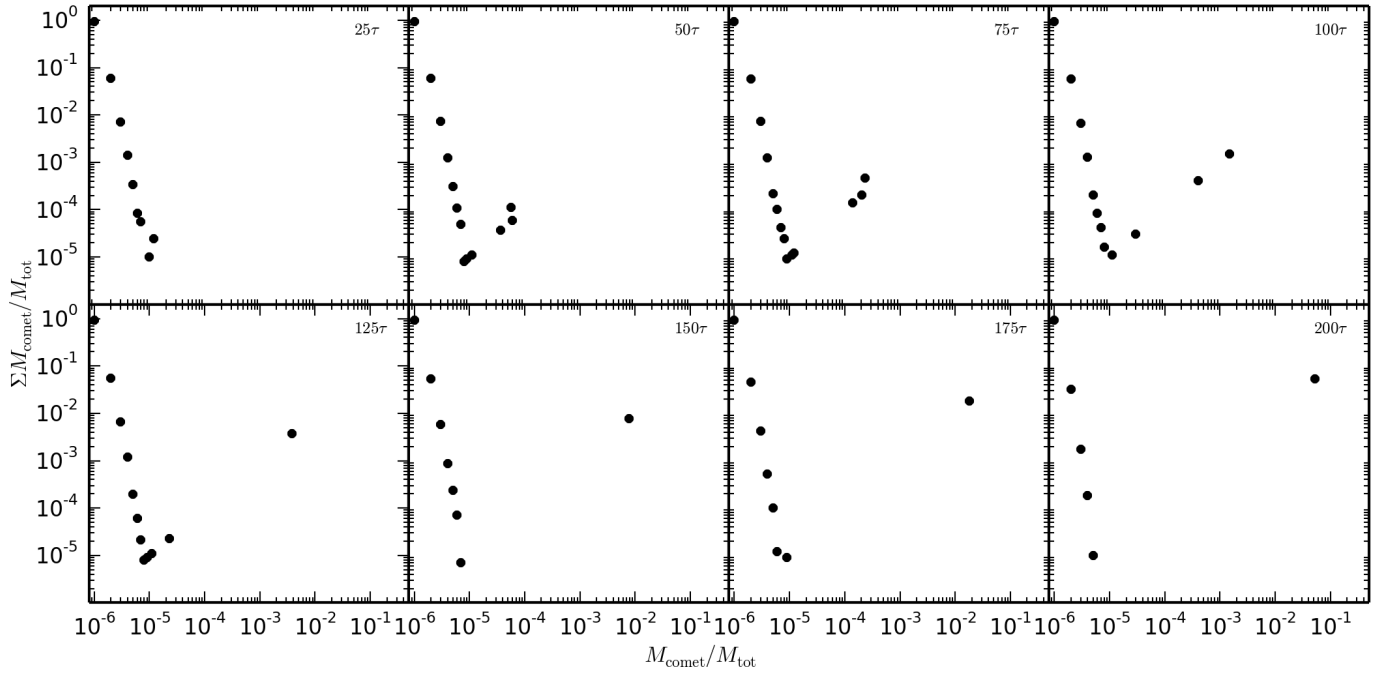


**Fig. 44.** “Comet” mass distribution of weakly self-gravitating simulation PT3-2 with  $N_{\text{SM}} = 100^3$ .